3-2023

Fast Engineering Model for Defect Production in Magnesium Oxide

Henry R. Little

FAST ENGINEERING MODEL FOR DEFECT PRODUCTION IN MAGNESIUM OXIDE

THESIS

Henry Little

AFIT-ENP-MS-23-M-094

DEPARTMENT OF THE AIR FORCE
AIR UNIVERSITY

AIR FORCE INSTITUTE OF TECHNOLOGY

Wright-Patterson Air Force Base, Ohio

AFIT-ENP-MS-23-M-094

FAST ENGINEERING MODEL FOR DEFECT PRODUCTION IN MAGNESIUM OXIDE

THESIS

Presented to the Faculty

Department of Engineering Physics

Graduate School of Engineering and Management

Air Force Institute of Technology

Air University

Air Education and Training Command

in Partial Fulfillment of the Requirements for the

Degree of Master of Science in Nuclear Engineering

Henry Little, B.S. Physics

March 24, 2023

AFIT-ENP-MS-23-M-094

FAST ENGINEERING MODEL FOR DEFECT PRODUCTION IN MAGNESIUM OXIDE

THESIS

Henry Little, B.S. Physics

Committee Membership:

Chris Lenyk, Ph.D
Chair

Darren Holland, Ph.D
Member

Adib Samin, Ph.D
Member

Abstract

Defect production from irradiation of materials with thicknesses much less than the mean free path for neutron interaction has been extensively explored, but the capability to predict damage for actual experimental conditions and timescales is lacking. Experimental measurements are expensive, taken over time scales of minutes to days, and limited to long term effects, while computational models are severely limited in either tractability or scope, with most simulations unable to simultaneously exceed micron scale physical dimensions, microsecond scale timescales, and single digit keV input energies. A method of accurately and inexpensively bridging the gaps between computations and experiments is explored using the well-studied material magnesium oxide and a simplified model based on bulk parameters and a reduced set of equations. The Monte Carlo N-Particle transport code (MCNP) from Los Alamos National Laboratory is used to simulate irradiation of a magnesium oxide rod using the Oak Ridge National Laboratories' High Flux Isotope Reactor (HFIR) neutron spectrum, tracking the neutron collision locations, kinetic energy changes, and identifying primary knock-on atoms (PKA). MCNP outputs the energy deposition from each simulated neutron collision via the particle track output (PTRAC) module. Using these results, molecular and cluster dynamics calculations predict defect production, and output the total number of F-centers resulting from the irradiation event. A defect formation rate per neutron is determined and defect saturation theory is applied to produce a relationship between neutron dose and defect concentration in the material for neutron doses 10^{14} – 10^{19} n/cm^2. The result is a model based on existing computational research which efficiently and accurately predicts the concentration of atomic defects under conditions closely matching experiments. Results are produced by the model

in 6.9 minutes using a single Intel® Core™ i7-10870H CPU running at 2.20 GHz, and comparison to the experimental data shows agreement within a factor of one to two depending on dose. Collision cascade size and homogeneity of defect distribution are identified as the most likely sources of remaining disagreement. The widely accepted theoretical formulation of defect production by Norgett, Robinson and Torrens is compared against an older formulation by Kinchin and Pease in the model, and the Kinchin-Pease formulation is found to produce stronger agreement with the inclusion of the ionization limit L_C. Inelastic scattering is identified as a large source of error for neutron energies > 1 MeV. The accuracy and computational performance achieved in this study for the investigated experimental scenario shows great promise for future development of this technique and unifying the simulation-experimental gap.

Table of Contents

Page

List of Figures

List of Tables

FAST ENGINEERING MODEL FOR DEFECT PRODUCTION IN MAGNESIUM OXIDE

I. Introduction

1.1 Background

Radiation damage in materials has been a subject of great concern for many engineering fields c. 1950, with myriad applications in defense, energy, electronics, and more. Over time, a strong understanding of the mechanics of radiation has been accumulated, as well as of its macro and microscopic effects on materials. Despite what progress has been made, however, there is a significant gap between what has successfully been modeled through computational predictions and experimental measurements.

The term "radiation damage" may take on many different meanings, however in this case it refers to the displacement of atoms in a solid from their original structure by radiation. This kind of damage can generally only be caused by mass-carrying types of radiation such as heavy ions, protons, neutrons, and to a lesser extent, electrons. A heavy particle which collides with an atom transfers kinetic energy, and, if the lattice atom's threshold displacement energy (TDE) is exceeded in the transfer, the atom is able to escape the potential well created by the surrounding material. The ways which this energy transfer is modeled depend on the type of radiation, the energy available to the system, and the scale of the system. In literature, scale is broadly defined using three categories: macroscopic, mesoscopic, and microscopic. Macroscopic objects are resolved over multiple mean free paths. The mean free path

refers to the distance a particle moving through a material travels, on average, before colliding. The mean free path depends on the energy of the moving particle relative to the target material, and to properties the material in question, so the generic length scales of macroscopic materials are ambiguous, as mean free path lengths can vary widely. In general, materials on the macroscopic scale are convenient to approach using the continuum approximation, wherein a material is modeled as a continuum rather than a collection of distinct atoms. The microscopic scale is, by contrast, marked by material thicknesses for which resolution of individual atoms or subatomic particles becomes significant - typically nanoscale or smaller. Finally, the mesoscopic scale describes a regime of intermediary sizes between nanometer and micron thicknesses. Even on the microscopic scale, there is considerable complexity in accurately modeling the time evolution of an atomic displacement by radiation in the context of its surroundings. Nevertheless, the accumulation of many of these interactions and their time evolution in a material causes changes in the material's macroscopic properties. The difficult, multiscale nature of this problem, both spatial and temporal in nature, has cultivated a broad scientific community connecting several otherwise independent fields of study [1–5].

Of the types of radiation capable of producing defects, neutrons in particular have been studied extensively in experimental work for their relevance to energy and defense applications. Many techniques, such as optical absorption, deep level transient spectroscopy (DLTS), and electron spin resonance (ESR), are only suitable for understanding and mapping the defect environment minutes to months after irradiation to ensure enough time has elapsed for radioactive isotopes to have safely decayed away [6–17]. This is in part due to the historic preference for experimental irradiations aimed at assessing material damage from high neutron doses to be conducted using nuclear reactors. While reactors have been designed which permit tailoring of the

neutron energy spectrum seen by the sample, a sample irradiated to a high neutron dose using a reactor is exposed to a wide spectrum of neutron energies over minutes to hours before being removed and inspected. This approach fails to capture the early-time evolution of defects as they are produced in the material by irradiation, and is only capable of investigating the material's long term response.

Computational models directed at defect production and evolution have approached the problem from the microscopic scale. Of particular interest are atomistic models: these simulate the collisions of individual neutrons with atoms in a lattice, accounting for structure and interatomic potentials - called the primary knock-on atom (PKA) - as the neutron imparts its energy. The trajectory of the atom through the material is modeled, along with the damage caused to the surrounding region. These models, in contrast to experiments, have proven limited in the scope of damage they can handle, evident in their applicable time scales, material volumes, and neutron energies [1, 18–23].

For broad application in industry and academia, codes such as Monte Carlo N-Particle (MCNP) and GEANT have been developed for general purpose use in solving problems of particle transport through materials, with sweeping scopes of potential applications including reactor moderation, criticality calculations, prompt radiation dosimetry from weapons, radiotherapy, and much more. These codes rely on Monte Carlo random sampling methods to produce statistically accurate results from simulations consisting of many individually transported particles. This approach sacrifices microscopic details such as the particular arrangements of atoms in materials for speed, but for its macroscopic applications still achieves quite accurate results. As a part of these microscopic concessions, these codes do not approach the problem of collisional damage in materials. Materials are modeled as continua with no regard for the microscopic crystal structure using the concept of interaction cross-sections,

or probabilities of interaction determined from bulk measurements. Damage to the material is not rigorously addressed; in particular, displacement of nuclei and their evolution in time is not modeled at all.

1.2 Motivation

Historically, the need for an understanding of defect evolution in devices has not been large. This can be seen in the development history of codes such as MCNP, which has never broached the topic since its inception [24]. This is due to the typical size regimes in which design takes place, and the effects of individual defects on the properties of macroscopic objects. For devices or design elements larger than a few mean free paths, understanding radiation damage at an atomic level is not relevant: one can get by simply observing and characterizing trends which appear at the macroscopic scale without ever broaching the details of crystal structure and displacement effects. Moreover, materials need not be treated as ordered lattices of atoms, but may instead be represented as continuous. These treatments work well for any macroscopic object of concern, however their success is predicated on the assumption that the material behaves as a bulk. The bulk assumption is that the material is sufficiently large that it is both continuous and infinite with respect to surface and boundary effects. This assumption is valid for many targets of interest, such as a rod of uranium, the wall of a reactor, or the door of a Humvee. As technology continues to advance, however, many electronic elements are becoming smaller and smaller. Transistors in particular are extremely small and expected to continue to shrink, with TSMC announcing a 3 nm transistor for 2022 and Samsung announcing a 1.4 nm transistor slated for 2025 [25, 26].

The radii of atoms are measured on the order of tens to hundreds of pm. Transistors with thicknesses in the low nm range are thus on the order of tens of atomic layers

thick. Such instruments call into question the bulk assumption on which analyses of radiation effects on devices have historically been based, with Knudsen numbers on the order of millions. The Knudsen number is defined as the ratio of the mean free path to a representative length scale, and any value greater than one suggests the continuum approximation is invalid. Compounding this concern is the fact that for a device whose thickness can be measured in atomic layers or lattice parameters, the displacement of one of those atoms has a much larger relative impact than when the bulk assumption is valid and the material can be considered macroscopic. For any application, it is vitally important to be able to produce realistic characterizations of the phenomena present. It is similarly important in the course of design to be able to repeatedly perform these preliminary analyses - this requires a method that is fast, inexpensive, and accurate. No methods or models currently exist which satisfy these criteria with respect to radiation effects on small electronic devices.

1.3 The Problem

Despite many approaches made to extend atomistic models out to realistic time scales, there does not yet exist an approach for fast prediction of neutron damage in a material which experimenters and designers can use to rapidly survey potential scenarios. Existing computational methods extending molecular dynamics without compromising microscopic detail are limited to shortened time scales in varying material solids to the range of 10^{-12} to 10^{-6} s [19–21, 27–29]. Reduced sets of cluster dynamic equations and simplified models have shown promise for extending the temporal studies of defect evolution with reasonable accuracy to experimental results, but still prove to be computationally expensive for use in experimental and design workflows [1, 30, 31]. Moreover, these types of models have never been used to replicate realistic neutron spectra, only simulating single-energy neutron sources, and are

further unable to reach the large neutron doses potentially relevant to design applications. The intervening gap that links current computational models and experimental observations requires attention to more accurately bridge between transient and long term responses for materials to effects of combined radiation environments. Of particular importance is the need for efficient surveying techniques for rapid analysis when material dimensions, such as those for microelectronics found on modern printed circuit boards, are well below the mean free path for radiation interactions. This work presents a framework for such a model, based on converging the accuracy of atomistic models, the speed of transport codes, and the underlying theory of defect production, to produce estimates of defect concentration resulting from neutron irradiation of a MgO crystal, matching the conditions of a real nuclear reactor and experimental data. The use of a continuum approach with MCNP serves to evaluate the usefulness of bulk-determined quantities such as interaction cross-sections for sub-mean free path applications.

1.4 Hypothesis

The goal of this research is to formulate and test a computationally simple model capable of predicting broadly the intensity of atomic level radiation damage resulting from neutron irradiation of a crystal. By combining the results from molecular dynamics simulations with defect evolution theory and existing particle transport codes, a simple and efficient prediction of material damage caused to a sample by a realistic neutron spectrum can be made. Comparing this prediction to experimental results should provide preliminary insight into the effectiveness of this method of converging fields of study at producing a realistic result. While each of these constituent elements arises from rigorous study, it remains to be seen whether their sum can produce a result consistent with what has been measured.

1.5 Methods

The ionic crystal MgO is selected as the target material for how extensively it has been studied by both the experimental and computational communities. Baseline data are taken from the atomistic simulations of Uberuaga et al. for determining the damage caused by neutron collisions in the lattice [19–21]. Theory developed by Kinchin and Pease is used to extend these results across a wide range of neutron energies [32]. The particle transport code MCNP is used to simulate the irradiation of a MgO sample, using the PTRAC module to extract data on a collision-by-collision basis [33]. Python code is used to interpret and process the data, and the results are compared against data recorded from experimental irradiations performed in the Oak Ridge High Flux Isotope Reactor (HFIR) Hydraulic Tube System (HTS) [11, 12].

1.6 Research Objectives

At present, while there simultaneously exist many experimental and computational studies in the literature approaching the problem of defect creation and evolution from the long term and short term directions, respectively, a concerted effort has not been made to connect the two. In particular, the results of cluster dynamics simulations carried out in ideal, microscopic environments have not been scaled and validated against experiments conducted in ideal, but comparatively realistic, scenarios. Accordingly, the primary research contributions of this work include:

- Prediction of defect concentration in a MgO crystal of sub-mean free path thickness subject to a reactor neutron spectrum using cluster dynamics results and theory calculations, and subsequent validation against experimental results
- Proof of concept for a fast computational model capable of surveying atomic level radiation damage

- Evidence to support the validity of MCNP, the continuum approach, and cross-section data in the sub-mean free path regime
- Exploration of factors contributing to inaccuracy between computations of defect evolution and experimental measurements

II. Background and Literature Review

In this section, the theory and models underlying the defect prediction model will be explained in detail. The model combines analyses of neutron irradiation and damage in magnesium oxide primarily from five sources: experimental defect measurements on irradiated samples; Monte Carlo neutron transport using MCNP; defect production theory; molecular and cluster dynamics simulations; defect saturation theory. The ordering of elements in this chapter reflects their order of relevance to the model in Ch. III.

The focus material of this research is MgO. MgO is appealing for the extensive catalog of experimental and computational studies investigating it, which will be discussed in detail below. MgO is an ionic simple cubic crystal, belonging to the space group $Fm\bar{3}m$, with lattice constant $a_0 = 4.26$ Å and a band gap of 7.7 eV [34].

2.1 Neutron Interactions with Matter

To begin investigating the damage resulting from neutron irradiation in magnesium oxide, the means by which neutron irradiation causes damage must first be addressed. Broadly speaking, the event of two particles passing nearby and inducing measurable change in one another's internal states or trajectories is defined as an interaction. When the extent of an interaction occurs over a relatively short amount of time, it is further defined as a collision. There may be defined two states in any collision: the initial constellation, before the collision has occurred, and the final constellation, after it has concluded. Collisions may then be subdivided between scattering collisions and reactions. Scattering collisions, in which the final constellation differs from the initial constellation either not at all or only by the excitation of the internal states of its members, may be elastic or inelastic. Elastic scattering collisions require

that the sum of kinetic energy present in each constellation remains the same, while inelastic scatters are characterized by the transformation of part of the initial kinetic energy to internal energy among the colliding particles. The kinematics of elastic scattering events can be modeled simply by classical "hard sphere" collision between the neutron and the nucleus, with energy transfer dependent only on their relative masses, velocities, and recoil angle. Reactions are defined as collisions for which the initial and final constellations are not not identical, leading to the distinction that inelastic scattering collisions fall under the reaction umbrella. In general, the factors which govern reactions are not trivial, and depend on the particular characteristics of the involved particles [35, 36].

The interaction of neutrons with matter has long been useful to model as probabilistic. Used to measure this probability is the cross-section for a particular type of collision. The number of a type of collision that occurs per unit volume per unit time depends directly on the number density of moving particles, the number density of target particles, and the velocity of the moving particles. The constant of proportionality which relates these quantities is called the microscopic cross-section, which has units of area and is typically given in barns, or 10^{-24} cm^2. The cross-section is often conceptualized as the apparent size of the nucleus to the passing neutron, but in reality is somewhat more complicated. When radiation theory was first being developed and the first experiments were being conducted, the difference in scale between isolated collisions and matters of practical interest was large; furthermore, isolation of single constellations to directly investigate interactions was infeasible. Experiments would involve large fluxes of neutrons passing through bulk volumes of material, and a quantity was needed to represent collision probability [35, 36].

The cross-sections for all interactions depend heavily on the energy of the neutron relative to the target nucleus. This energy dependence is nontrivial, and is so

important that an entire field of study has developed around the measurement and tabulation of neutron cross-sections, the intricacies of which are beyond the scope of this work. All cross-section data used in this work are sourced from the Evaluated Nuclear Data File (ENDF)/B VII.1 library, developed and released by the Cross-Section Evaluation Working Group on December 22, 2011 [37]. Fig. 1 shows a comparison of the total microscopic cross-sections of Pu-239, an isotope which has undergone meticulous study for decades, and Mg-24, relevant to this work and relatively less studied in the nuclear field. Cross-section plots by energy can be divided into three distinct regions: thermal, fast, and resonance. The thermal region is the low energy region where the total cross-section is at its largest. In nuclei where absorption is energetically favorable, the thermal region is where it would most probably occur. Conversely, the fast region corresponds to high energy neutrons. In the fast region, the elastic cross-section is usually constant, with other cross-sections decreasing proportionally to the inverse of neutron velocity. In between these two is the resonance region. Resonances typically correspond to energies where absorption or excitation are particularly favorable, and manifest as sharp peaks in cross-section. In Fig. 1, the resonance region for Pu-239 is relatively well defined, while for Mg-24, there are fewer and often wider peaks. Also worthy of note is the energy range at which resonances begin; in Pu-239 and other heavy elements, this region is situated in the eV range, while for light elements it appears in the MeV range [36]. It is important to consider that nuclear resonances are still actively researched, and especially in the case of less studied isotopes, new resonances are still being discovered. Models relying on nuclear cross-section data can only be as accurate as these measurements. The cross-sections shown for Mg-24 are characteristically similar to those of O-16, Mg-25, and Mg-26, the other isotopes relevant to this work.

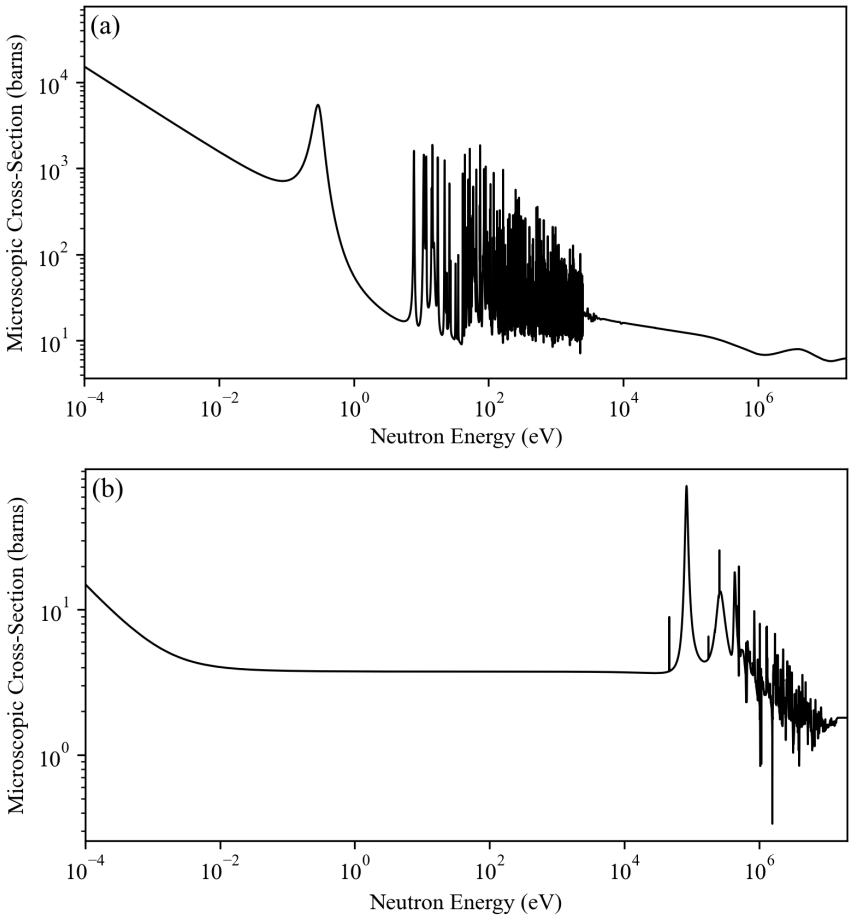

Figure 1: Comparison of neutron total microscopic cross-section data between Pu-239 (a) and Mg-24 (b). Cross-section data in this work are sourced from the ENDF/B VII.1 library, released by the CSEWG on December 22, 2011 [37].

2.2 Reactor Irradiation

The experimental irradiations being compared against in this work were performed in the Oak Ridge High Flux Isotope Reactor (HFIR) Hydraulic Tube System (HTS). The HFIR is outfitted with several experimental irradiation facilities, each designed to produce a different radiation environment. The normal reactor cycle is 23 days, which would be a limiting factor to experiments requiring very high neutron flux over short time periods were it not for the HTS [38]. The HTS is a system which can be used to remotely insert experimental samples into the core of the reactor while

it is running: aluminum capsules called "rabbits" are loaded with materials to be irradiated and hydraulically lowered into the flux trap. These rabbits are cylindrical, and have an interior space defined by r = 0.255 in., h = 2.562 in. The neutron spectrum at this location is provided in Fig. 2. This spectrum was recorded in 1971 by Kam and Swanks, and has since changed with the transition from the HFIR from a highly enriched uranium to low enriched uranium, however the experiments being compared against were conducted before this switch [39–42]. The total flux in the HTS with this spectrum is 5×10^{15} n/cm^2. Across this volume at the location within HFIR, the neutron spectrum is reported to be invariant [38, 43].

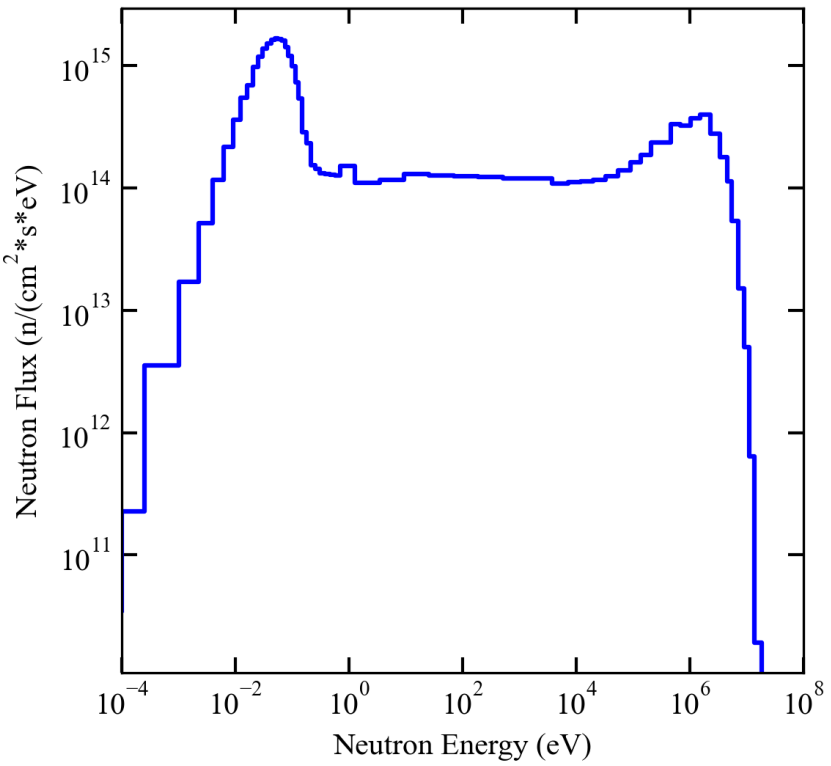

Figure 2: Neutron spectrum in the Oak Ridge HFIR HTS [39]. The total neutron flux is 5×10^{15} n/cm^2, with the highest measured neutron energy being 18.3 MeV.

2.3 Experimental Techniques

Experimental validation of defect evolution resulting in stabilized isolated centers from irradiation in MgO has long been studied and characterized with techniques such as electron paramagnetic resonance (EPR) and deep level transient spectroscopy (DLTS) [6–9, 13, 15–17]. Early experimental work by Kingery and others [10, 44] revealed that radiation induced defects had not only a temperature dependence, but also that several different defects were present after an irradiation. Their work also suggested an agglomeration of defects during irradiation and an annealing of radiation-induced defects at the ambient temperatures (i.e. defect recombination). Other studies of the long-term effects of electron and neutron irradiation on defect formation and evolution by Chen et al. [11] have shown defect stability to at least 900° C (approximately 2.53 eV). Work by Halliburton et al. [15, 16] definitively identified cation vacancies induced by neutron and high-energy electron irradiation with thermal stability on the order of years. Additionally, oxygen interstitials were observed by Halliburton et al [15, 16]. Evidence for anion vacancies after irradiation was presented by Nelson et al. [17] in his work on shocked materials.

The irradiation results used to compare this model against, however, were obtained using absorption spectroscopy [11, 12]. Absorption spectroscopy, at its simplest, involves measuring the attenuation of light as it passes through the material of interest. Often, and as is the case with MgO, there exist absorption "bands" in the material corresponding to particular wavelengths which are absorbed preferentially. In MgO, which is transparent when pure, absorption bands appear in the material following irradiation. These bands correspond to particular defects which accumulate in the material - the 250 nm absorption band corresponds to the F-center in MgO. F-centers are defined as anionic vacancies occupied by one or more unpaired electrons, and will be the defect species focused on in this work. Derived by Sibley and Chen is an

equation which relates the measured absorption coefficient of this band to a concentration of F-centers in the material [45]. This equation is an application of Smakula's equation, a generalized relationship derived in 1930 to describe the optical absorption of defects which has been foundational in experimental defect measurements [11, 12, 45–47]. Both experimental data sets referenced in this study used this equation to produce their results.

In both experiments, single crystals of MgO were investigated, meaning there were no grain boundaries between crystals present in the samples. Further care was taken to select samples for irradiation which had grown with high purity. Nevertheless, some impurities in their samples were inevitable - these impurities have the potential to throw off measurements, especially when their concentrations are similar or greater than the concentration of the defect in question. A summary of irradiations and observed defect concentrations is shown in Tab. 1, while the full data along with their original plots are presented in appendix A.

Table 1: Summary of experimental defect concentrations by neutron dose. Experimental data included come from the experiments done by Chen et al. and Mcgowan and Sibley [11, 12].

Neutron Dose (n/cm^2)	Defect Concentration (n/cm^3)
3.50×10^{14}	3.60×10^{16}
4.05×10^{15}	2.91×10^{17}
2.00×10^{16}	1.00×10^{18}
1.50×10^{17}	2.70×10^{18}

2.4 MCNP

The spectrum from the HFIR HTS is used to sample neutron energies irradiating a simulated target in the model. The MCNP 6.2 software is used to simulate neutron irradiation of a MgO sample and output neutron collision information. MCNP is a proprietary software developed by Los Alamos National Laboratory (LANL) based

on the theory of Monte Carlo particle transport through continuous material geometries. The fundamental theory of Monte Carlo is predicated on building an estimate of the deterministic solution to a problem by sampling on its distribution a large number of times. In the case of particle transport, this is modeled by simulating the histories of a number of particles, from a birth condition to a termination condition, and typically involves several random variables - the particle's starting energy, its direction, the path length of the particle before an interaction, the type of interaction, the energy deposited, secondary particles produced, etc. All of these random variables are contributing factors to the true distribution of the problem's solution, and as the number of particle histories simulated increases, this solution should resolve itself more clearly. This approach is often preferred over deterministic methods for its comparative tractability, but in practice comes with many limitations. Fundamentally, the number of histories run and the corresponding variance in the final answer are only indicative of the statistical precision of the simulation results. The physical accuracy of a Monte Carlo solution is bounded not only by statistics, but also by the physicality of the presented problem and the physicality of the model being used; one may achieve a solution with nearly zero variance, but which was predicated on unrealistic assumptions or nuclear data.

MCNP 6.2 is a professional Monte Carlo particle transport software, and has a staggering suite of capabilities, ranging from criticality safety calculations to structural moderation analysis to medical applications and more [33]. In an account given by Goorley et al., the theory behind Monte Carlo particle transport codes began to catch traction in the 1950's and 60's with the development of several independent codes at LANL [24]. In 1973, the Monte Carlo Neutron Gamma (MCNG) code was developed by merging independent neutron and gamma transport codes Monte Carlo Neutron (MCN) and Monte Carlo Gamma (MCG). MCN was at the time the latest

neutron transport code developed by LANL and was designed to be as general as possible [48]. MCN handled neutron transport through systems of geometries defined by the user from sources similarly defined by the user. Neutron interactions were predicated on cross-section data provided by Lawrence Livermore National Laboratory. Unlike in modern MCNP, cross-section data were not modified in any way and were simply linearly interpolated on to determine interaction probabilities. The MCNG code would later be merged with the low energy photon code, Monte Carlo Photon (MCP), resulting in the first iteration of MCNP - at this point standing for Monte Carlo Neutron Photon [24]. The code would later be added onto by Sandia National Laboratories to enable electron transport as well, and subsequently more and more particle types, becoming the modern Monte Carlo N-Particle code.

With decades of additions and refinement, MCNP 6.2 is the state of the art for simulating macroscopic neutron transport. It supports the construction of immensely complex geometries and the input of virtually any conceivable material composition, with physics underpinned by extensively developed cross-section libraries. Depending on the rigor desired from the simulation, MCNP 6.2 can simulate neutrons, photons, electrons, protons, heavy ions, and other particles concurrently. Radiation source specification allows for point, surface, or volume sources based on the geometry of the problem, and source sampling is customizable with respect to particle direction, energy, and distribution across the source. A host of pre-defined tallying routines are provided by the software for analysis. These routines range in complexity from counting neutrons in the specified volume, to calculating deposited energy, to reporting criticality values, and more. Tallies in MCNP are analyzed by the software using a host of checks for statistical precision, and statistical uncertainty is reported automatically alongside each tally output. Despite the extensively detailed physics involved, MCNP 6.2 remains highly optimized and efficient, employing a wide range

of techniques to streamline problems and improve statistics based on the desired output, including variance reduction to reduce the number of histories needed to achieve a statistically precise result.

Despite MCNP's many strengths, a gap exists with respect to the needs of this investigation. MCNP 6.2 does not simulate the crystal structures of materials, treating them as a continuum. MCNP determines when and where interactions occur using input libraries of microscopic cross-section data, by default using ENDF libraries formatted for use using the Nuclear Data Processing System (NJOY) code. As touched on in Sec. 2.1, these measurements do not represent the full breadth of physics involved in a neutron interaction, but are convenient and accurate for determining macroscopic cross-sections and MFP's, for use in the macroscopic regime. This lack of detail is recognized and specifically desired for this investigation. An assessment of the accuracy of MCNP and a continuum based approach for microscopic damage predictions is highly valuable to the development of a robust damage surveying tool.

Used alongside tallies in this study is the Particle Track Output (PTRAC) module. Tallies are a convenient way to shed the cumbersome storage issues presented by Monte Carlo, by creating a running sum for some quantity of interest, and discarding all other information produced for each particle history. This method allows MCNP to run vastly more efficiently and permits many more histories to be run than would otherwise be able to be stored in memory without consuming gigabytes of space. Before modern advancements in digital storage, when the parent codes for MCNP were conceived, this was essential to successfully employing Monte Carlo. For decades, MCNP had no built-in functionality to retain all of the information generated in each neutron history. The PTRAC module is a recent development, allowing for this storage in a separate output file. As predicting defect concentration is predicated on individual collision cascades, the specific energy depositions and locations of all

neutron collisions are necessary for the model in this work. Unfortunately, the use of the PTRAC module requires that all data processing and statistics be implemented manually. Additionally, the number of histories which can feasibly be run is severely limited, with a storage requirement at 10^9 histories between the orders of hundreds to thousands of GB. The PTRAC module is receiving vast performance improvements with the release of MCNP 6.3 - unfortunately this update was made after this research had completed.

2.5 Atomic Displacement Theory

The MCNP PTRAC output provides a list of energy depositions which are used to calculate defects using atomic displacement theory and computation results. When a neutron scatter occurs off of a lattice nucleus, there is a minimum kinetic energy transfer requirement to lift the target nucleus out of its potential well. The barrier it must overcome varies due to several factors, but is fundamentally the result of the material's bond structure and the sum of forces acting on the atom from the rest of the lattice. While a fully detailed explanation is far beyond the scope of this paper, this energy requirement, commonly referred to as the threshold displacement energy (TDE), varies with material composition and crystallographic direction of recoil. In most materials, the TDE is of the order of tens of eV, and has been taken to be 25 eV when otherwise unknown in early work [32]. Over the course of MgO's study, the TDE's for oxygen and magnesium have been investigated extensively both experimentally and computationally. From an experimental perspective, many different values have been found for both elements; for oxygen, values are reported ranging from 44 to 60 eV, while values for magnesium are clustered between 60 and 64 eV [7, 9, 49]. Importantly, the crystallographic direction is not always specified in these results, so comparison between them is questionable. Computational studies

have found TDE's to vary over a much wider range, with the TDE's of both oxygen and magnesium varying between 40 and 160 eV depending on the direction of recoil [18–21, 50, 51]. Recommended average values vary from 47 and 41 eV respectively by Williford et al. to 67 and 90 eV by Park et al. The molecular dynamics simulation results used in this paper, discussed in detail in Sec. 2.6, take the values to be 65 and 90 eV, respectively. Suffice it to say, the true value of the TDE varies considerably by recoil direction, and is not widely agreed upon in the literature. A table providing a summary of TDE measurements is provided in appendix B.

The first widely accepted theoretical basis for defect production from various forms of radiation was formulated by Kinchin and Pease in 1955 [32]. Treating neutron-nucleus and interatomic collisions as hard sphere collisions, and assuming a moving atom slows down primarily due to collisions with other stationary atoms, Kinchin and Pease developed an early formulation for predicting neutron damage. They predicted that a collision event will produce a cascade of displacements depending on the energy transferred in the original collision, and that the total number of displaced atoms will depend linearly on the energy of the primary knock-on atom (PKA) and the TDE. The energy transfer is modeled classically, and the resulting number of defects produced is as follows:

$$E_{max} = \frac{4M_1M_2}{(M_1 + M_2)^2}E \tag{1}$$

$$N_d = \frac{E_{max}}{4E_d} \tag{2}$$

Here E_{max} is the maximum energy transfer possible from the scattering event, M_1 is the mass of the moving particle, M_2 is the mass of the stationary target, and E is the energy of the neutron. In this case, M_1 refers to the mass of the neutron, and M_2

to the mass of the nucleus. N_d, then, is the total number of defects produced by the resulting collision cascade, with E_d representing the minimum displacement energy of the PKA. It follows that for an energy transfer below $4E_d$, no defects are expected to be produced. While an interstitial-vacancy pair (Frenkel pair) may be produced with lower energy transfer, the resulting interstitial is not energetic enough to escape the immediate vicinity of the vacancy it has created, and recombines immediately.

For very high PKA energies, another interaction becomes important to consider - the energy binding electrons to lattice nuclei. An atom traveling with sufficient energy will begin to strip electrons from surrounding atoms along its path, thereby losing energy without creating additional displacements. The energy threshold at which a PKA begins stripping electrons is represented below by the quantity L_C:

$$L_C = \frac{1}{16}\frac{M_1}{m}\epsilon_0 = \frac{1}{16}\frac{M_1}{m}\pi a_0^2 E_R (3N_0\sqrt{\pi})^{2/3} \tag{3}$$

Here m refers to the mass of an electron and ϵ_0 to the Fermi energy of the freed electrons. a_0 is the lattice parameter, E_R is the Rydberg energy and is equal to 13.6 eV, and N_0 is the number of atoms per unit volume in the material. This is called the ionization limit, and introduces nonlinearity to the total number of defects produced for PKA energies above it. A second relationship for N_d at energies above L_C is thus presented:

$$N_d = \left(2 - \frac{L_C}{E_{max}}\right)\frac{L_C}{4E_d} \tag{4}$$

Shown in Fig. 3 is the nonlinear behavior introduced by the ionization limit to the otherwise linear defect trend line. It can be seen that above L_C, the number of defects produced is drastically impacted, and energy loss to ionization rapidly becomes a dominant phenomenon. The L_C term depends on several parameters which vary

depending on the material, namely the number density of atoms, the mass of the target nucleus, and the lattice parameter. Shown in Fig. 4 is the impact of varying number density and PKA mass on the number of defects produced by PKAs of one, two, and three MeV. A similar trend is exhibited by both plots, where increasing the parameter in question increases the number of defects produced up to a peak value, after which it begins to decrease. The highest possible number of defects produced increases linearly with PKA energy. From observation of Eq. 3, the ionization limit is directly proportional to mass, and proportional to number density by the cube root of its square - this is the cause of the slightly differing shapes between the two curves.

This set of relationships would become a baseline for the community when evalu-

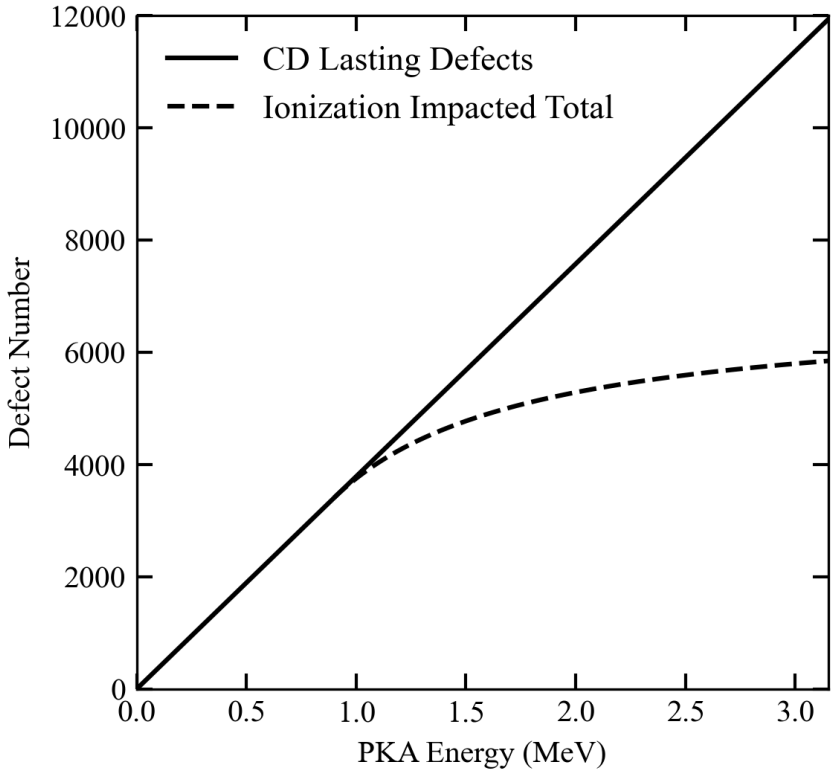

Figure 3: Showcase of the impact of ionization limit on defect production. The trend line produced using the atomistic simulation results is augmented by Eq. 4. Ionization severely limits additional defects produced in the high energy regime.

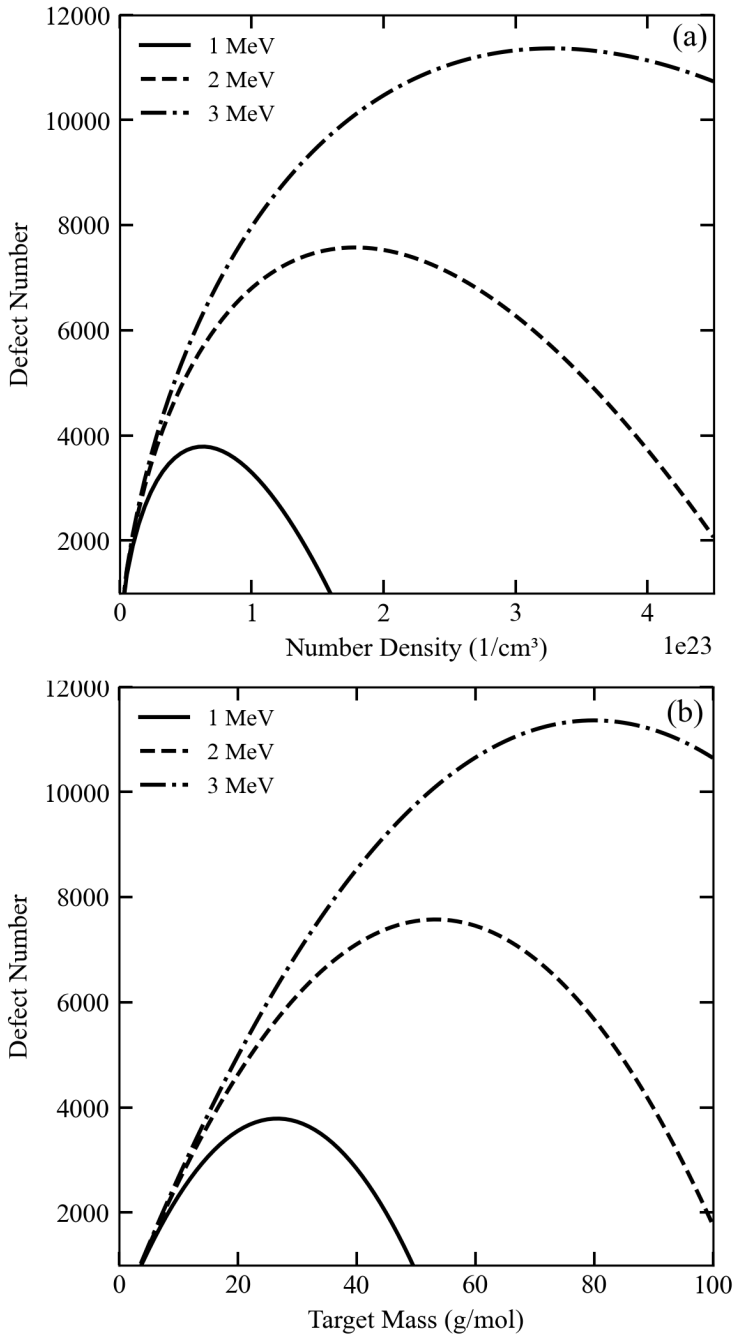

Figure 4: Effects of varying number density (a) and target mass (b) in Eq. 3 for three transferred energies. Both plots show a similar relationship. There appears to be a value in each case which maximizes defect production in the material. This value increases, along with the maximum number of defects produced, with PKA energy.

ating neutron damage in crystals, but left considerable room for improvement, often failing to produce accurate predictions when compared against experiments and in-depth simulations. The model would later be refined by Norgett using simulation results by Robinson and Torrens as well as a semi-empirical derivation by Nelson, resulting in the now commonly used Norgett-Robinson-Torrens (NRT) model [1, 17, 52]. This model, shown below, introduces a factor κ representative of the displacement efficiency, a quantity which attempts to account for the tendency for interstitials to instantly recombine:

$$N_d = \frac{\kappa(E - \hat{Q})}{2E_d} \tag{5}$$

The value of κ is determined to be a constant equal to roughly 0.8, except for energies near $2E_d$. The quantity $\hat{Q}$ represents the energy lost in the collision cascade to ionization, and acts to effectively combine the two equations provided by Kinchin and Pease for above and below the ionization limit. The difference between E and $\hat{Q}$ represents the total energy available in the system to create atomic displacements. This version of the Kinchin and Pease (KP) formulation is what is used today, though it still proves ineffective on its own at predicting the damage produced in a material from irradiation. This formulation also completely neglects the nonlinear effects of the ionization limit on large defect cascades, a shortcoming which has been overlooked by the community for its better standalone agreement with experiments at lower energies. For this reason, the KP model is used in the algorithm over NRT. A discussion is provided in Sec. 4.5 addressing this choice in further detail.

2.6 Atomistic Simulations

Atomistic simulations are any of a broad range of computation techniques aimed at studying the behavior of materials subject to perturbations at the atomic scale.

The model in this paper is produced using the results of such a simulation. A full explanation of all atomistic simulation methods is beyond the scope of this work, however an explanation focused on cluster dynamics, a technique used in the study informing this model, is provided below.

The study of cluster dynamics builds on the early displacement theory through the use of detailed, atomic-scale simulations to predict transient material damage with collisional models. These simulations provide finely detailed results describing not only what types of defects are formed but where they form and how they evolve over time in the material. In the case of traditional simulation methods, this detail comes at the cost of computation speed, and such simulations are limited to predictions out the the order of picoseconds before computation time becomes prohibitively slow.

A brief overview of the fundamentals of cluster dynamics is provided by Kohnert et al. [28]. The study evolved from the earlier Mean Field Rate Theory (MFRT), developed in the 1970's. MFRT is based on solving a set of differential equations describing the continuous rates of change of the concentrations of vacancies and interstitials in a material subject to irradiation. The cluster dynamics method came about as an extension of this model to account for defects of orders greater than single interstitials and vacancies, which MFRT could not. The balance equation used by cluster dynamics may then be expressed,

$$\frac{dC_n}{dt} = -\nabla \dot{J}_n + g_n + R_n(\overrightarrow{C}) - D_n k_n^2 C_n, \tag{6}$$

for n defect species of interest. C is concentration, J is the flux of the given species, g describes defect production during recoil events, D is the species diffusion coefficient, and k^2 describes the strength of sinks for removal of defects. $R_n(\overrightarrow{C})$ is more involved, represented as follows:

$$R_n(\overrightarrow{C}) = \sum_{i+j\to n} k^+_{i,j} C_i C_j - \sum_{\substack{i+n\to m \\ n+i\to m}} k^+_{i,n} C_i C_n + \sum_{\substack{m-i\to n \\ m-n\to j}} k^-_{m,i} C_m - \sum_{n-i\to j} k^-_{n,i} C_n \quad (7)$$

$R_n(\overrightarrow{C})$ generally accounts for the interactions of clusters in the system with one another. The formation of species n is governed by the first and third terms, accounting each for combination of smaller species and dissociation of larger species into n, while the second and fourth terms describe the corresponding losses from n. In principle, this expression can be taken broadly to account for many orders of clusters or narrowly to only consider low order defects, with the choice of scope affecting the computational tenability of the problem but providing new depth of insight into the behavior of a material subject to irradiation. Crucially, this model may additionally be expanded to allow for explicit spatial resolution, providing insight into the effects of defect arrangement on their development over time.

Traditional cluster dynamics calculations rapidly become intractable for situations of high doses and volumes, as the number of equations involved increases exponentially with additional species [28]. Both in response to this issue and independent of it, several alternative models and methods have been conceived which circumvent or mitigate this problem. The next most computationally difficult is a group of approaches collectively described as Kinetic Monte Carlo (KMC) methods. As described by Stoller et al., KMC is predicated on the complete simulation of the crystal lattice, wherein every point defect and defect cluster has an explicitly defined location within a finite simulation cell [53]. Under irradiation, defects are simply introduced to the cell at discrete locations and times. The behavior - mobility, combination, dissociation, etcetera - of defects within the volume is simulated directly using kinetic Monte Carlo. KMC methods avoid the combinatorics issue of traditional cluster dy-

namics, but are still computationally restricted to very small problem sizes relative to experimental scales. The explicit simulation of the crystal lattice typically limits KMC to cell volumes < 100 nm across, which results in poor resolution at the experimental scale and increases in computation time exponentially [22]. The concepts of KMC inspired a Monte Carlo approach to the traditional cluster dynamics equations, resulting in stochastic cluster dynamics (SCD) [54]. Discretization and stochastic integration of the cluster dynamics equations allows for a substantially faster solution to large volume problems, but still struggles with high species count [28]. An alternative approach was contrived to instead reduce the number of equations needing to be solved, using a grouping scheme, however this approach trades accuracy for efficiency, neglecting correlations as the problem evolves [55, 56]. While some more than others, all approaches to reducing complexity of cluster dynamics calculations succeed at improving their efficiency for large simulations. Despite all these advances, however, there still does not exist a commonplace method for efficient predictions that are readily comparable to experiments. While successful in incorporating great detail, cluster dynamics models for the time being remain limited in their capacity to cover broad energy spectra, large volumes, and high doses.

Despite their shortcomings, cluster dynamics models have contributed immensely to the modern understanding of radiation effects in materials. Indeed, existing results of cluster dynamics models may be leveraged in bridging the gap between simulation capability and experiments. In this work, the results of a set of simulations by Uberuaga et al. are implemented alongside the defect production theory of the previous section to inform the number of defects produced by each neutron collision simulated [19–21]. These particular simulations apply a combination of multiscale methods following their initial cluster dynamics to extend their results out to time scales approaching those observed in experiment, including temperature-accelerated dynamics

and density functional theory. Collision cascades were simulated for three different PKA energies: 400 eV, 2 keV, and 5 keV. 20 cascades were simulated at 400 eV, while 12 were simulated at 2 and 5 keV. Uberuaga et al. report results as totals across all simulations for each energy. They include the total number of displacements which occur along with the number of defects lasting longer than 8 ps. Additionally, they provide a breakdown of the types of defects produced, however this information is largely beyond the scope of the model developed in this work. Notably, they find that there is no strong preference in collision cascades for displacements of cations or anions, a detail which becomes useful for comparison with experimental results that will be discussed further in chapter III. The simulation findings of interest are presented in Tab. 2, averaged per neutron for each energy.

Table 2: Simulation results taken from Uberuaga, 2004. In this context, defects refer to Frenkel pairs. All reported values are averaged per neutron. Reproduced with permission from Uberuaga and Physical Review [19]

PKA Energy (keV)	Displaced Atoms	Post-Collisional Defects
0.4	9	0.5
2	48	7
5	124	18

2.7 Defect Saturation

The final element to the model is the concept of defect saturation. When a material is subjected to very high doses of heavy particle irradiation, the rate of defect formation decreases until the material is saturated, at which point defect concentration becomes constant with dose. The increasing density of vacancies, interstitials, and resultant defect cascades begins placing transient and more stable defects in closer proximity [57]. This has been modeled using the concept of a "forbidden volume," inside which recombination will immediately occur if a vacancy is present. This concept is also used in cluster dynamics models, referred to by that community as the

capture radius. A set of equations is presented by Henderson and Bowen for neutron irradiation of magnesium oxide, based on experimental observations [13]:

$$F(t) = F(\infty)\left(\frac{t}{t+\tau}\right) \tag{8}$$

$$F(\infty) = \frac{2}{v} \tag{9}$$

$$\tau = \frac{F(\infty)}{\left(\frac{dF}{dt}\right)_0} \tag{10}$$

where t is dose, F is defect concentration, and v is the forbidden volume. The forbidden volume is determined to be a sphere of radius nearly nine times the lattice constant for MgO based on experimental results [13]. The initial formation rate of F+ centers, $(dF/dt)_0$ depends on the energy or spectrum of energies of the incoming neutrons and scales linearly with fluence. In the model presented here, $(dF/dt)_0$ is determined using the theory and molecular dynamics results of sections 2.5 and 2.6. The equations above were developed specifically for F-centers, making their use for comparison against experiments convenient. It is additionally assumed that the temperature is within a range where interstitials are mobile and the F-centers are not [57]. In magnesium oxide, the temperature at which the F-centers become mobile is of the order $400°C$, which makes this assumption reasonable for most applications [13].

III. Methodology

The methodology described in this chapter combines the detailed results of an MCNP neutron transport simulation with the results of an atomistic simulation study and atomic displacement theory to survey long-lasting radiation damage in MgO rods. The methodology described in this chapter leverages MCNP's excellent neutron transport capability to accurately mimic the irradiation conditions of two experiments conducted at the Oak Ridge HFIR. The results of a cluster dynamics study are combined with atomic displacement and defect saturation theory, and applied to the collision information recorded from MCNP. A flowchart for the defect prediction method is shown in Fig. 5. This methodology produces an estimate of defect concentration over a range of input doses for an experimentally relevant scenario in a short amount of time, and in the results chapter is validated against corresponding experimental data.

The flowchart describes a linear process for the model with three distinct stages before experimental comparison. Beginning with MCNP, a neutron transport simulation is run based on the irradiation conditions of the relevant experiments. The results are then output using the PTRAC module, which writes particle by particle information to a large output file. The second stage of the model begins with the processing of this output file in Python. The energy deposition of each collision is converted to a defect total using the atomistic study results and kinematic defect theory. The resulting defect total is converted to defect concentration over neutron dose using the output of an integrated neutron flux tally from MCNP. Finally, saturation theory is applied in the process of scaling this initial concentration to dose ratio to experimentally relevant doses. The results of this process are plotted against the experimental data for analysis.

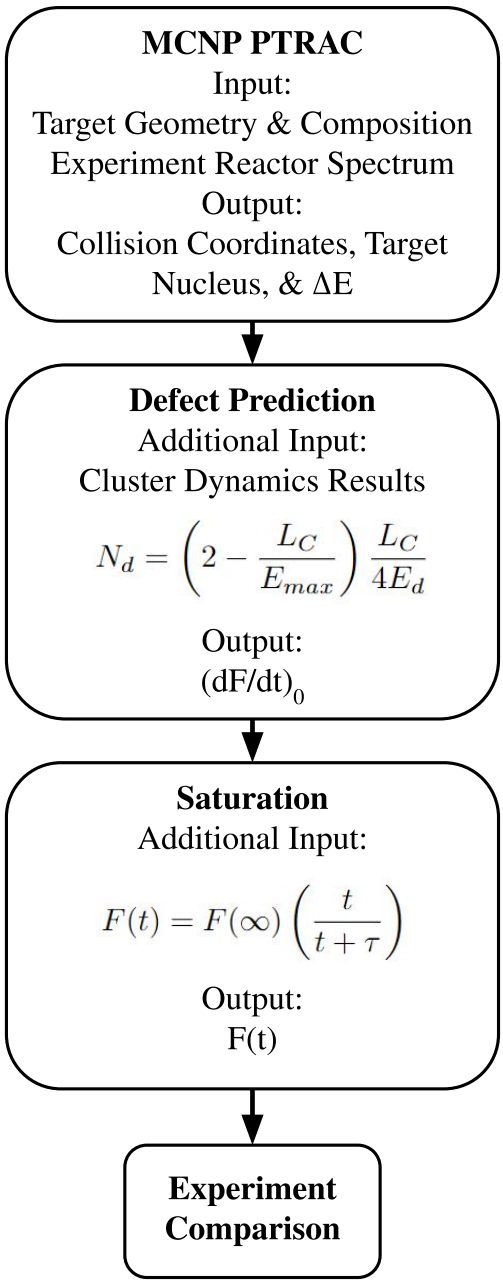

Figure 5: Flowchart indicating the steps in the defect prediction algorithm. The algorithm begins with the MCNP simulation, incorporating the irradiation conditions of the experiments. From MCNP's PTRAC module, collision information is output and processed using a python script. The trend line from Uberuaga et al. is paired with the theory for reduced cascade size at high energies to determine the initial rate of defect formation, $(dF/dt)_0$. Finally, saturation theory is applied and the result is scaled to relevant doses, for comparison against the experimental data.

3.1 Experimental Data

Before any steps of the model's process could be performed, the experimental conditions and data had to be determined. The magnesium oxide rods in each experiment were cleaved from single crystal grown by W. and C. Spicer Co. Ltd., with lengths ranging from 0.5 cm to 1 cm, and cross-sectional dimensions ranging from 0.01 cm^2 to 0.1 cm^2. The placement of the rods within the rabbits in the HTS was not specified in either experimental paper; furthermore, the presence and arrangement of other materials potentially affecting the neutron spectrum inside the rabbits was also not discussed. Rods were irradiated for times ranging from minutes to days, and measurements were made within an hour of removal from the reactor. Optical absorption measurements were made and the magnitude of the 250 nm absorption band was used in conjunction with following equation to determine the concentration of F-centers in the sample,

$$fn_F = 4.0 \times 10^{15} \alpha_{250}, \tag{11}$$

with $f = 1$ [11, 12]. Samples were optically bleached before absorption band measurements were made.

Data from the experiments were extracted from plots using the WebPlotDigitizer software since the tabulated data were unavailable. The particular plots extracted from may be found in referenced papers by Chen et al. and Mcgowan and Sibley [11, 12]. Shown in Fig. 6 is the interface of the software used to extract the data. The user manually indicates the axes of the plot, as well as two reference points on each axis to establish scale. The software can be set to assume the plots are log scaled. The user must then place an overlaid marker on each point on the figure to tell the software where the relevant data are in the image. At any point, the user may view

the coordinates of each overlaid point and export them as a CSV file. A zoom feature and pixel-by-pixel adjustments are supported to maximize precision when aligning axes and distinguishing points. In total, 32 points were extracted across the two experiments.

In McGowan and Sibley's experiment [12], data from two plots had to be matched up to align neutron dose with reported F-center concentration. The first plot depicted increase in flow stress over neutron dose, and the second increase in flow stress over concentration of F-centers. The data were extracted from each plot and matched together, showing agreement to within 5%. This error was determined by taking the difference observed when matching the data of the two plots together, and represents the fidelity of the software used to extract them. Chen et al. [11] reported neutron dose against the intensity of the 250 nm absorption band, and the concentration of F-centers had to be calculated. The data were extracted and attributed with a

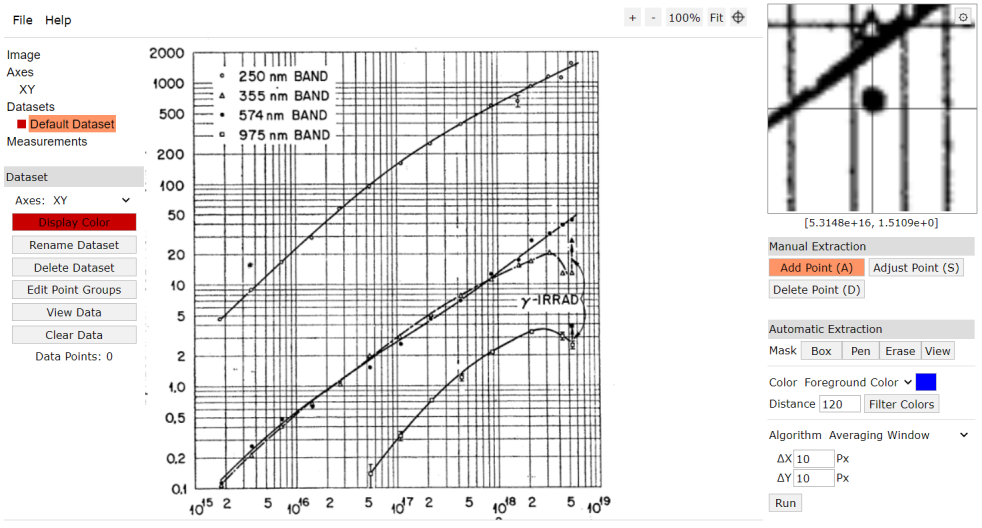

Figure 6: GUI of the WebPlotDigitizer software. The user begins by importing an image and identifying four points on the image to align the axes, with the option to treat either axis as log scale. The user may then select points on the image, with the aid of the top right window. Once the desired points have been selected, the precise coordinates of these points relative to the user defined axes are reported using the "view data" option. The plot in this image was reproduced from Chen et al. [11]

relative error of 13%, dominated by the error reported in the paper. Tab. 1 previously discussed in Sec. 2.3 shows a snippet of the extracted data, while the full tables are included in appendix A.

The neutron spectrum used in the simulation was measured in the HFIR HTS in 1971 by Kam and Swanks, and is shown in Fig. 2 in Sec. 2.2. It should be noted that this spectrum was measured for Hydraulic Tube (HT) 5, while the experiments in question were both conducted in HT-12. These locations are all located within the flux trap of the reactor. The spectrum at each location is considered uniform based on the flattened flux profile of the reactor [39]. The spectrum was determined using transport theory computations to calculate the neutron energy and flux spectra, then compared against selected monitors for validity. The results of the calculations and measurements are reported to be within 10% agreement.

3.2 MCNP Setup

As outlined in Fig. 5, the first stage of the model is the MCNP neutron transport simulation. MCNP 6.2 was used to simulate neutron irradiation of MgO samples under nearly identical conditions to the experiments. Mimicking the experimental geometry in MCNP required that assumptions be made regarding several parameters of the experiments, due to their absence from the corresponding papers. From the size of the cavity inside the rabbit, it was assumed that absent any complicating interior geometry, the neutron spectrum and flux are uniform. The choices of the containment geometry and composition were not specified, and so assumed to be arbitrary. The geometry was thus chosen to be a magnesium oxide block of dimensions 1 cm $\times$ 0.01 cm^2, suspended in a spherical vacuum cavity of radius 0.51 cm, to minimized the complexity of the simulation. The choice to fill the cavity with void, rather than air, was made to minimize complexity in the PTRAC output file. While the interior of

a rabbit is not a perfect vacuum, this assumption is valid with the understanding that the measurement of the spectrum was made at the same location, and so should include any effects caused by the presence of air. The neutron energy spectrum used was recorded at the same location in the reactor, so to match the experiments, the rod must be subjected to an isotropic flux of neutrons with identical energies. The choice of cavity shape was made to maximize efficiency by reducing geometry specifications. This radius was chosen to maximize neutron flux through the block, in order to minimize the number of neutrons needed in the simulation. Neutron starting position was sampled uniformly across the spherical surface, and neutron direction was sampled isotropically in the azimuthal direction. The cosine of the angle between the neutron's direction of flight and the normal vector to the surface was sampled from 0 to 1. This effectively mimicked the random paths of neutrons in the HFIR HTS facility, but resulted in many source neutrons missing the MgO block entirely, which had to be considered when evaluating statistics of the final result. The material composition of the block was chosen based on the compositions of natural magnesium and oxygen. Natural magnesium is 79% Mg-24, 10% Mg-25, and 11% Mg-26, making an isotopic breakdown necessary for accuracy. The composition of the sample in MCNP was specified to be 39.5% Mg-24, 5% Mg-25, 5.5% Mg-26, and 50% O-16. The energy spectrum of the neutrons was input as a probability density function with bins defined by the report of Kam and Swanks [39]. The binned nature of the reactor spectrum means that changes in the sampling probability by energy occur abruptly at specified intervals. This suggests that for j energy bins, there exists a spread of energy ΔE_j over which the sampling probability is uniform. Due to the nature of energy transfer due to downscattering, the input spectrum is multiscale with energy, and its energy bins are defined on a logarithmic scale. This results in the energy spread ΔE_j increasing for higher j. To prevent this nonuniform bin width from

distorting the sampling probabilities of energies in wider bins, the input spectrum was normalized taking the integral over the data provided by Kam and Swanks. An f4 tally from MCNP, evaluating integrated flux across a specified surface, was employed for the MgO rod in order to convert simulation results from number of histories to dose. The integrated flux normalized per neutron was determined to be 1.223 cm^{-2} with a statistical uncertainty of 0.03%, and was multiplied together with the number of histories to determine the dose to the rod. The input deck is provided in Appendix C.

The PTRAC module was used to write every particle event in the simulation to a separate output file. A simulation of 10^8 histories produced output files of 60 GB, prohibitive for work on a single machine; therefore, 10^7 histories were typically run to save time and space. Results from the PTRAC simulation are later scaled to experimentally relevant doses between 10^{14} and 10^{19} n/cm^2. While the PTRAC card in MCNP allows for customization of its output to mitigate file size, no optimization options were sufficient accommodate all of the information desired for analysis. PTRAC files contain full details on every event which occurs in a given simulation, and thus require bulk processing to interface with efficiently. From each neutron collision, the target nucleus, the incoming neutron energy, the outgoing neutron energy, and the XYZ coordinates in the sample were desired. A python script was developed to process an input PTRAC file and output a CSV file containing the listed information for each neutron collision that occurred - this processing reduced the file size of a 6 GB PTRAC file to a 3.5 MB CSV file. While the uncertainty in the f4 tally is straightforward to quantify using MCNP's built-in statistics, any uncertainty originating from the PTRAC data must investigated manually.

3.3 Uncertainty

Two major sources of uncertainty are introduced by this stage of the simulation: cross-sections and statistics. The cross-sections, taken from ENDF/B-VII.1, are tabulated with associated uncertainties, however the format of ENDF files is challenging to interpret and requires a significant time investment to properly handle. Additionally, the processing and doppler-broadening of these cross-sections with NJOY introduces further uncertainty to the data used by MCNP. Rather than attempt to directly investigate the uncertainty included in the ENDF files, a comparison test was performed in the interest of time. The ENDF/B-VII.1 cross-section library was compared against the ENDF/B-VIII.0 library for otherwise identical simulations, and the defect totals predicted across 10 different seeds were compared. The maximum variation observed between defect totals on identical seeds was 5.1%, with an average variation of 3.2%. This suggests reasonable agreement between the data of each library and that the cross-section data may be considered reliable. This study is heavily limited due to a lack of data for the Mg-25 and Mg-26 isotopes. These are the only two libraries supported by the MCNP community which contain complete data for these isotopes. While other libraries exist with cross-section data for Mg-25 and Mg-26, use of them in MCNP would first require labor intensive processing beyond the scope of this work. A worst-case error of 5.1% in the defect total predicted is assumed to result from the cross-section data used this study.

Statistical uncertainty arises in both the f4 tally result and the PTRAC data. The statistical uncertainty in the f4 tally is consistently $< 0.1\%$. The resolution of the energy distribution of the HFIR spectrum is the largest contributor to statistical uncertainty in the PTRAC data. For speed of simulation and practical implementation on a single machine, achieving a result with sufficient precision using simulations of 10^7 histories was desirable. The statistics produced by this number of histories

required investigation to ensure low uncertainty resulted from this choice. Statistical uncertainties $< 1\%$ were desired to ensure the history count was not prohibiting accuracy of the simulation. Based on the input spectrum, incident neutron energies > 3.4 MeV have very low probabilities to be sampled, and present a potentially large source of uncertainty in the defect total produced. A linear combination approach was used, simulating 10^7 neutrons per bin, to ensure proper representation of each bin. Based on counting statistics, where uncertainty is defined as follows:

$$\sigma = \sqrt{N} \tag{12}$$

the statistical uncertainty within each source bin was calculated. here σ is the absolute error in observation N. The uncertainty introduced by source bin representation from this method was 0.7%. This was sufficient to conclude that statistical uncertainty would not play a major role in the overall uncertainty of the final defect total.

Conducting a complete analysis of uncertainty in the final defect concentration prediction of the model inclusive of error from MCNP as well as in the defect prediction model is considerably more involved than what is presented above, and was not performed in this work. Consideration would need to be given to the measurement uncertainties of all physical parameters included in the model, many of which do not have uncertainties explicitly provided. The uncertainty contributions from each of these parameters would need to be propagated through the model to develop an estimate of the uncertainty in the number of defects predicted for an individual neutron collision. This uncertainty would also depend on the input energy, which informs what operations are performed, and as a result, what parameters are involved. This would then be coupled with the MCNP input to produce a defect total with an uncertainty depending on the statistics in MCNP, the operations performed by

the defect prediction model, and the physical parameters involved in that prediction. This result would still neglect uncertainties in the cross-section data employed within MCNP. An incomplete attempt to characterize uncertainty in the defect total is provided in Appendix D, making several assumptions to simplify the process. A more comprehensive uncertainty analysis is recommended as future work.

3.4 Post-Processing

The remaining stages in Fig. 5 were carried out in a collection of post-processing scripts. The Python programming language was used with multiple general-purpose libraries for all post-processing and data analysis, mainly for its versatility as a data processing platform. Overall, the code can be broken up into three stages: reading, initialization, and analysis. At the first stage, the code reads the PTRAC output file and picks through for collision information, discarding everything else. The initialization then involves calculating several quantities of interest, including the number of defects associated with each collision, and outputting an expanded table. These two stages comprise the "defect prediction" stage of Fig. 5. Finally, using this table, several modules allow for various investigations into the data, as well as the application of the saturation stage and comparison against experimental results. The full code is included separately, with a detailed description provided below.

3.4.1 PTRAC Reading

The first step of post-processing is to parse and trim the PTRAC output file into a CSV file containing only the desired information. Shown in Fig. 7 the bulk of a PTRAC file is organized as a sequence of particle histories, with each particle's history described by a sequence of events. The first digit in a particle history will be the number of the particle, followed by the source event tag. The following lines are

grouped in pairs, with each pair of lines corresponding to a new event and containing all of the information describing it. The beginning number in the first pair of each lines is a flag identifying an event type. Unlike all other information in the given pair of lines, this flag corresponds to the end of the track segment described in that pair of lines, rather than the beginning. This means that the flag indicating a collision is not situated in the same two lines as that collision's information, but two lines earlier. The parsing script operates by opening the file line by line, searching for the 4000 flag, corresponding to a collision event. Once the flag is detected, it saves its position, opens the next three lines, and extracts the collision position, nuclide, and energy deposited, before returning to its original position and continuing through the file.

Fig. 7 is useful for examples. The first history shown, #74, is one of the most common types seen in a typical output file, and one which the parser script completely ignores. Line one indicates that the particle is born, with its history number followed by the 1000 flag. It completely misses the MgO rod in its trajectory, eventually intersecting with the edge of the problem geometry, indicated by the single 3000 flag for intersection with a surface in the problem geometry. This is followed by the 5000 flag, indicating termination of the neutron, and finally the 9000 flag, terminating the history. The position information of the particle at birth is contained in the first three numbers on line three, below the 3000 flag, and its position at termination is given in line five. The information in line seven is identical to that of line five, repeated to indicate that both the neutron and the history were terminated here. Since this history contains no 4000 flags, the parser script ignores it.

The second example, #75, begins again with the source flag. The neutron intersects with the MgO rod, indicated by flag 3000, and the surface designator 10.4 (cell 10, surface 4) in the third column two lines below (line 11). The neutron then

```
     74      1000
   3000         1        40        20         0         0
 0.69315E-01 -0.30284E+00 -0.40446E+00  0.81110E-01  0.88084E+00  0.46642E+00  0.89196E-06  0.10000E+01  0.00000E+00
   5000         2        20        28        30         0         0
 0.14228E+00  0.48952E+00  0.15116E-01  0.81110E-01  0.88084E+00  0.46642E+00  0.89196E-06  0.10000E+01  0.68863E+02
   9000         2         1         1        30         0         0
 0.14228E+00  0.48952E+00  0.15116E-01  0.81110E-01  0.88084E+00  0.46642E+00  0.89196E-06  0.10000E+01  0.68863E+02
     75      1000
   3000         1        40        20         0         0
-0.85332E-01 -0.34216E+00  0.36844E+00 -0.54656E+00  0.53346E+00 -0.64552E+00  0.27486E-07  0.10000E+01  0.00000E+00
   4000         2      10.4       122        10         1         0
-0.38466E+00 -0.50000E-01  0.14902E-01 -0.54656E+00  0.53346E+00 -0.64552E+00  0.27486E-07  0.10000E+01  0.23884E+03
   3000         2      8016         2        10         1         1
-0.39729E+00 -0.37673E-01 -0.15350E-04  0.66612E+00 -0.41192E+00 -0.62178E+00  0.34717E-07  0.99995E+00  0.24891E+03
   3000         3      10.4        65        20         0         1
-0.37736E+00 -0.50000E-01 -0.18623E-01  0.66612E+00 -0.41192E+00 -0.62178E+00  0.34717E-07  0.99995E+00  0.26053E+03
   5000         4        20        37        30         0         1
 0.37499E-01 -0.30654E+00 -0.40586E+00  0.66612E+00 -0.41192E+00 -0.62178E+00  0.34717E-07  0.99995E+00  0.50219E+03
   9000         4         1         1        30         0         1
 0.37499E-01 -0.30654E+00 -0.40586E+00  0.66612E+00 -0.41192E+00 -0.62178E+00  0.34717E-07  0.99995E+00  0.50219E+03
     76      1000
   3000         1        40        20         0         0
-0.12944E+00  0.49293E+00 -0.19004E-01  0.29693E+00 -0.95489E+00  0.43492E-02  0.24229E-07  0.10000E+01  0.00000E+00
   4000         2      10.3       162        10         1         0
 0.82968E-02  0.50000E-01 -0.16986E-01  0.29693E+00 -0.95489E+00  0.43492E-02  0.24229E-07  0.10000E+01  0.21545E+03
   4000         2      8016         2        10         1         1
 0.27997E-01 -0.13352E-01 -0.16698E-01  0.36507E+00 -0.66476E+00 -0.65178E+00  0.32837E-07  0.99995E+00  0.24626E+03
   3000         2      8016         2        10         1         2
 0.39235E-01 -0.33815E-01 -0.36762E-01 -0.10405E-01 -0.59974E-01  0.99815E+00  0.23987E-07  0.99991E+00  0.25855E+03
   3000         3      10.5         3        20         0         2
 0.38330E-01 -0.39028E-01  0.50000E-01 -0.10405E-01 -0.59974E-01  0.99815E+00  0.23987E-07  0.99991E+00  0.29912E+03
   5000         4        20         5        30         0         2
 0.33592E-01 -0.66340E-01  0.50455E+00 -0.10405E-01 -0.59974E-01  0.99815E+00  0.23987E-07  0.99991E+00  0.51171E+03
   9000         4         1         1        30         0         2
 0.33592E-01 -0.66340E-01  0.50455E+00 -0.10405E-01 -0.59974E-01  0.99815E+00  0.23987E-07  0.99991E+00  0.51171E+03
```

Figure 7: Example set of histories from the PTRAC output file. Histories numbered 74, 75, and 76 are shown. Each history begins with its number, and '1000' indicating the particle being born. Each subsequent track segment terminating in an event is described by a pair of lines. The first number at the first line of each pair indicates the type of event terminating the track segment: 3000 corresponds to crossing a cell boundary, 4000 to a collision, 5000 to a history termination, and 9000 to the final entry in a history. Note that while these initial flags describe the event at the *end* of the current track, the rest of the information contained in the line pair describes the *beginning* of the track, resulting in some nuance in automated file processing. The other important numbers are as follows: the third number of the first line describes the starting surface or point of the track, which, following a collision, is the ID of the nuclide collided with; the first three numbers of the second line are the particle's XYZ position; the seventh number of the second line is the neutron's energy.

undergoes a collision, indicated by flag 4000 in line 11. This triggers the parser, and it opens lines 12-14. Again, the third column two lines below in line 13 indicates the target, in this case 8016 (O-16). The initial and final energies in this collision are given in column 7 of lines 12 and 14, respectively. The position of the collision is given by the first three entries of line 14. After processing these three lines, the parser returns to line 11 and continues. The neutron then passes out of the rod and terminates.

The third example introduces an important complication. History #76 undergoes

two back to back collisions, identified on lines 24 and 26. Lines 26 and 28 identify the target nuclides, 8016 in both collisions. The initial and final energies of the first collision are given in lines 25 and 27, while those of the second collision are in lines 27 and 29. This introduces a problem, however, with common file reading schemes. Typically in data processing it is sufficient to read line-by-line, or block-by-block, discarding each block when it has been processed to save memory. Were that the procedure used here, the parser would identify the 4000 flag on line 24, read forward to extract its collision information, and in the process, overlook the second 4000 flag. This is why it is critical for the parser to save its position upon identifying a 4000 flag, and return after extracting data. All extracted data are written to a CSV file, with each line containing the information of a unique collision. The loop iterates until all lines in the file have been read.

3.4.2 Initialization

The remainder of the post-processing code is organized under the "PTRAC" class. When the class is instantiated, the user must specify the file path to a processed CSV file, and the data read-in by the PTRAC reader script are pre-processed in the initialization of the class object. The initialize function iterates through the PTRAC CSV file and determines the number of defects produced by each collision, using the theory discussed in Section 2.5 along with the cluster dynamics results presented in Section 2.6.

The main purpose of the initialization is to determine the number of defects produced by each recorded collision. Before reading any data, the function first sets up several preliminary variables. Many of these are storage tools to make later data processing more smooth, but two critical quantities are established at this point. The first is L_C, the ionization limit discussed in Section 2.5. This variable stores separate

values for Mg and O, which are later selected depending on the target nuclide identified by PTRAC. As discussed in Sec. 2.5, the NRT model does not handle collisions above the ionization limit realistically, so the ionization limit is handled with the original KP formulation. The second quantity is a linear inter/extrapolation function based on the data taken from Uberuaga et al. [19–21]. This will be the baseline for predicting the number of defects produced by a collision cascade, with situational modifications applied as necessary from theory.

For each collision, the handling of the deposited energy depends on which regime it belongs. Collisions depositing less than 350 eV create no lasting displacements, and are immediately discarded. Depositions between 350 eV and the ionization limit L_C of the target nucleus produce defects linearly with energy according to the cluster dynamics results. Depositions above L_C follow the nonlinear relationship defined by Kinchin and Pease in Section 2.5, adjusted to align with the cluster dynamics line [32]. This adjustment will be further discussed later. Finally, the energy deposited is compared against the maximum possible elastic energy transfer using the incoming neutron energy and the target nucleus. This check is important to determine if inelastic scatter occurred. There are several excitation levels in MgO to which an MeV-order neutron may scatter, however only the lowest three are explicitly handled in this work [58]. For these lowest 3 levels, if the energy deposition falls within a particular level's range, the variable storing the energy deposition is corrected down by the energy of the nuclear excited state to determine the kinetic energy transfer. Inelastic scatters to levels above the bottom three are discarded; reasons for this decision are discussed in Sec. 4.4.2. After calculating the defect contribution of each collision, the initialize function outputs the following information: the total number of defects; the total numbers of oxygen versus magnesium collisions; a trimmed array, containing all baseline information on each collision event which transfers enough

energy to produce a defect, along with the defects produced by each collision. This array also contains several additional quantities for analysis:

- The total number of displacements produced in each collision cascade, before any recombination occurs.
- The adjusted kinetic energy transfer.
- An integer counter identifying the source bin of the colliding neutron.
- A flag indicating whether the neutron was discarded for exceptional inelastic scatter.
- The defects produced by the collision squared, for the earlier discussed coefficient of variation analysis.

This information is all stored in the class object and available to its constituent methods. Once this information is determined, the user may call various methods from the PTRAC object to retrieve information, generate plots, or perform analysis.

The adjustment made to align the KP equation for defects above the ionization limit with the trend line produced from the cluster dynamics results requires attention. Referring to Sec. 2.5, the only quantity in the formulation of Eq. 4 which is not definitively known is E_d (a.k.a. the TDE); furthermore, this equation was formulated assuming a homogeneous material, and does not intrinsically support the existence of two TDE's. This requires that a single average TDE across the material must be chosen, a decision which is advantageous for several additional reasons. The discrepancies between the reported experimental and computational values make assignments of the individual displacement energies for Mg or O challenging. As discussed previously, MCNP also has granularity introduced through the PTRAC module which identifies the PKA and energy change of the incoming and outgoing neutron, but

not the individual collisions within the resultant cascade or the ionization. Bonding within the perfect MgO lattice is identical for each direction and therefore, variations in the displacement energy are primarily driven by the mass difference. Reporting has indicated that near equal interactions are expected between incident neutrons and either Mg or O at the energies expected to create stable defects [7, 13], further making definitive attribution of displacement energies difficult. In addition, the sample dimensions that are compared to the simulations are well below the mean free path for MgO. This characteristic may contribute to small variations in the TDE as a function of distance as the material begins deviating from bulk properties and assumptions of local potentials. The selection of an average displacement energy enables the circumvention of these limitations.

Eq. 4 was adjusted to align with the cluster dynamics line by equating the two at their connection point and solving for the TDE. This resulted in a predicted TDE of 66 eV. In theory, the result of such an adjustment should represent an average TDE for the material. Perhaps fortuitously, this value of 66 eV, compared alongside the predictions of TDE discussed in Sec. 2.5, appears to be quite a reasonable average. For comparison, the same procedure was used with the NRT model to investigate whether the NRT model would produce a TDE value closer to the experimental and computational predictions. The results of this investigation are presented in Sec. 4.5.

3.4.3 Experimental Comparison

The plotting of defect concentration as a function of dose for experimental comparison is the stage at which saturation is incorporated. Until this point, defect information has been stored as the total number of defects produced in the MCNP simulation against the number of histories; these must be converted to concentration and dose, respectively. The conversion from total neutrons to dose is performed using

the result of MCNP's f4 tally over the surface of the MgO sample, and concentration simply uses the volume. A baseline defect concentration per unit dose is determined this way, and then passed to the saturation equation. A slight difference arises in the code at this point from the discussion in Sec. 2.7. The saturation equation used is as follows:

$$F(D) = F(\infty)\left(\frac{D}{D+\tau}\right) \tag{13}$$

Where Eq. 8 is in terms of irradiation time, the code instead handles dose directly. In practice, these achieve identical results, however the treatment of irradiation time is more experimentally correct, while treatment of dose is more direct for computation [13, 57].

The experimental papers do not report the concentrations of total defects by dose, but the concentrations of F-centers by dose. It is thus necessary to determine the ratio of F-centers to other defect types produced by neutron irradiation. In the cluster dynamics case, a defect refers to a lasting frenkel pair, or an interstitial-vacancy pair which does not anneal out in the first 8 ps of its existence [19–21]. There is information in the cluster dynamics simulations regarding the number of oxygen and magnesium vacancies produced: in the 400 eV PKA shots, 3 oxygen monovacancies were produced and 1 magnesium; in the 2 keV shots, 33 oxygen and 30 magnesium; in the 5 keV shots, 78 oxygen and 80 magnesium. PKA's were split evenly between oxygen and magnesium, and these results indicate that as PKA energy increases, there is no clear preference in the collision cascade toward displacing oxygen over magnesium or vice versa.

The PTRAC results and cross sections used by MCNP were also investigated to determine if a preference exists for the PKA. The ratio of defect-producing collisions between oxygen and magnesium PKA's was 1:0.9, or 52% oxygen to 48% magnesium.

Interestingly, however, a comparison of the total neutron cross-sections between magnesium and oxygen in this energy range is instead 1:1.2, or 45.5% oxygen to 54.5% magnesium. The explanation for this difference is most likely the inconsistent scattering angles of incoming neutrons. A 5 keV neutron does not produce a 5 keV PKA; furthermore, whatever amount of energy it does transfer will not always be the same. This means the direct investigation of neutron cross-sections is less useful than the actual simulation results. Nevertheless, both these figures point toward the preference of PKA between oxygen and magnesium being about 50/50. Treating this as the case, a factor of 0.5 was applied to the defect concentration prediction to consider only anionic vacancies. With changes to this factor, the agreement with the experimental data changes linearly; unfortunately, without substantially greater detail in the model, the production of F-centers cannot be calculated directly. With this final correction, the simulation results may be plotted against the experimental F-center concentration measurements and compared.

3.4.4 Other Analyses

Several functions exist within the PTRAC class for additional analysis. These functions may broadly be divided into three categories: spatial, temporal, and collisional analyses. For spatial analysis, three different plotting schemes were used. All defect producing collisions were plotted spatially in a 3D scatterplot for preliminary inspection of their distribution. Subsequently, density plots were created along the X, Y, and Z centerlines of the sample. Densities were determined by dividing the sample along the axis of interest into rectangular segments. This method provides collision density in 1D along the axis of interest, which when analyzed for all 3 spatial axes, provides insight into the distribution of collisions around the edges of the volume relative to the interior.

The third function investigates the distribution of nearest neighbor distances between defect-producing collisions in the sample. This function was particularly challenging to implement efficiently, due to the exponential growth of operations the computer must perform with an increasing sample size. This growth forces the consideration of only a subset of the data, which creates an additional concern with respect to analysis. A user specified number of points is isolated from the larger dataset, and each point's nearest neighbor distance is calculated by iterating through all other points in the set. A histogram of the spread in nearest neighbor distances is produced for 10^4 defect producing collisions. In this case, considering fewer points not only weakens the statistics of the results, but also fundamentally changes the quantity being investigated. When the data set is smaller, the number of points within the considered volume is smaller, and so the average distance between points is larger. This phenomenon must be considered when analyzing the results.

For temporal analysis, a set of exponential decay plots is produced for each experimental point. The exponential curves are fit between three points: the total number of displacements before annealing predicted by the cluster dynamics, the later prediction of remaining defects, and the experimental measurement. This analysis encountered several issues, all discussed in detail in the next chapter. Finally, the collisional analysis entails several plots investigating the distribution of collisions for incident energy and deposited energy, including scatter plots and histograms.

IV. Results and Analysis

This chapter focuses first on an analysis of the model's output compared against the results of the experiments by Chen et al. and Mcgowan and Sibley [11, 12]. In the following subsections, several analyses are conducted relating to the main results, primarily focusing on disagreement with the model's prediction. Saturation behavior is investigated first, with macroscopic collision density and nearest neighbor distance analyzed for their potential impacts on the effects of saturation as dose increases. A temporal analysis is conducted to attempt to characterize time-dependent annealing in the sample and whether it not being considered substantially impacted the model's output. A broad investigation into the energy deposition outputs from MCNP identifies several peculiarities which are discussed. The choice of TDE and the impact of using the KP formulation over NRT in the model is investigated. Finally, the model is used to produce outputs for three additional neutron spectra to investigate the effects of changing the input spectrum and whether expected behavior is observed.

4.1 Simulation Results

The predicted concentration of defects in the MgO sample for a varying neutron dose is plotted against the experimental irradiations in Fig. 8. These results were produced using 10^7 histories, with the total time to produce the final defect calculation being 6.9 minutes on a single Intel® Core™ i7-10870H CPU running at 2.20 GHz. Damage is quantified in F-centers per cm^3, and also in displacements per atom (dpa). The prediction shows strong agreement with the experimental results for low doses $< 3 \times 10^{16}$ n/cm^2. Above 3×10^{16} n/cm^2 agreement weakens, to a peak overestimate within a factor of 2.2. Above 10^{18} n/cm^2, the experiments and the prediction agree more closely again, as both approach the saturation limit of MgO. As discussed pre-

viously, a full assessment of uncertainty on the simulation output was not conducted. Error bars are not plotted on the experimental data as they are smaller than the points themselves on the presented scale. The time to complete this simulation using only a single laptop renders it several orders of magnitude faster than the more involved cluster dynamics models typically used for defect analysis; furthermore, the results themselves are comparably accurate to currently existing methods for predicting bulk material damage out to long times.

For doses below 3×10^{16} n/cm^2, the strong agreement can be characterized by a lack of saturation behavior. The computational and experimental models each follow a similar linear growth pattern in this regime, with the experimental irradiations describing a slightly shallower slope in relation to dose than the computation. There is large variation in the experimental irradiations at low dose. These may be outliers, or they further indicate a mismatch in the true slope of F-center production in this region compared against the computation. Regardless, the strong agreement and linearity of this region suggest that for doses between 10^{15} and 3×10^{16} n/cm^2, the results of low energy, short time scale cluster dynamics simulations may be used in conjunction with an ionization limit model to accurately predict F-center concentration in MgO; furthermore, using a realistic neutron spectrum that incorporates a broad spectrum of neutron energies, it can be seen that the effects of F-center saturation are unimportant in this regime.

The experimental data show variations which clearly exceed the uncertainties quantified in Sec. 3.1. At the bottom of the range of experimental data, two points recorded by Mcgowan and Sibley stand out as outliers to the general pattern [12]. While a direct explanation is not given in their paper, they outline clearly that the chemical purity and dislocation content of MgO samples vary widely from crystal to crystal, and large variations may be expected to arise between samples as a result. It is

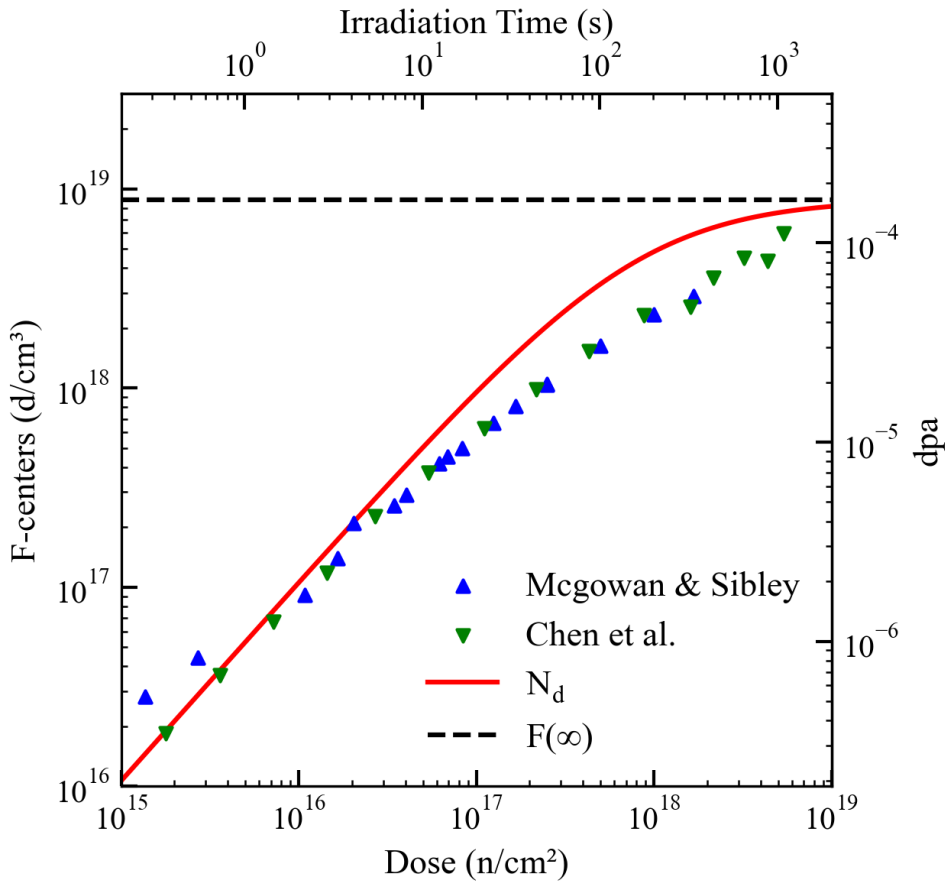

Figure 8: Comparison of the results of the model to the results of experimental irradiations performed by Chen et al. and Mcgowan [11, 12]. The saturation limit $F(\infty)$ is also included. Agreement is excellent for doses below 3×10^{16} n/cm^2. Between the regions of 3×10^{16} and 3×10^{18} n/cm^2, agreement worsens to within a factor of 2.2, before converging back toward the experiments near the saturation limit.

plausible that these compositional differences between samples are more pronounced in the low dose regime, where F-center concentration produced by irradiation is still relatively low ($< 10^{-6}$ dpa), and become less relevant as dose increases. This tracks with the general trend of the experimental data becoming more clustered as dose increases, with the exception of irradiations by Chen et al. near saturation dose [11]. This may again be due to the irregularities of experimental MgO samples, and to the effects of impurities in MgO crystals. Chen et al. present a table of impurity concentrations in a sample batch of MgO specimens, listing several elemental impurities

on the order of tens of parts-per-million (ppm), or 10^{18} nuclei/cm^3, including Ca, Al, Si, and Zn, along with several more elements in lower concentrations. Similar to the effects of doping on semiconductors, it is possible that the presence of so many impurities alters the structure of the potentials in the lattice, such that the saturation limit of the material is reduced on a specimen-by-specimen basis depending on the impurity profile.

Above 3×10^{16} n/cm^2, poor agreement as the model tends to overestimate defect concentration suggests that there are either inaccuracies in elements of the current model, or other unaccounted for phenomena. The following discussions will investigate potential sources of this disagreement. While the experimental irradiations follow a consistent, gradually decreasing slope with respect to dose from this point up to the saturation region, the computation largely retains its linearity until above 10^{17} n/cm^2, overshooting the experiments and then tapering off relatively abruptly as it approaches the saturation limit. This disparity suggests that there is some inadequacy in the handling of F-center saturation in the computation. It is proposed that this model would be improved with the accounting of interaction between defect cascades in the sample. Presently, no spatial resolution of defect cascades is accounted for by the model, and it is possible that as dose increases, defect cascades which are placed in close proximity to one another will have fringe interactions, contributing to an earlier onset of saturation effects than otherwise predicted. This potential explanation is further investigated in Sec. 4.2. Several additional possible sources of disagreement are discussed in further sections, including time-dependence, inelastic scattering, and the selection of an average E_d, along with other potential sources of inaccuracy.

4.2 Saturation

The most prominent question derived from the results of the computation regards the disparity between its saturation response and that of the experiments. Upon first review, a prime candidate for investigation was the macroscopic distribution of defects across the sample. Collision and defect density plots were produced along the x- y- and z-axes of the simulated sample, and the x-axis plots are displayed in Fig. 9. The y- and z-axis plots are not included, as they appear qualitatively identical. The extremely noisy appearance of these plots suggests that there is no spatial distribution preference across the volume, and defect producing collisions can be taken to be distributed randomly. This reinforces the idea that in the sub-mean free path regime, the distribution of neutron interactions across a given length of material will be uniform [22].

Related to the investigation of macroscopic defect density is the question of microscopic defect density. Even in the case of uniform defect distribution across the material, some defect cascades are closer to each other than others. As discussed previously, interaction between defect cascades and the resultant early onset of saturation effects is tied into this notion. The distribution of nearest-neighbor distances by frequency of occurrence was investigated to provide a better grasp on this phenomenon. As discussed in Sec. 3.4.4, the determination of nearest neighbor distance is a difficult computation problem to optimize. This investigation focused on an initial computation for nearest neighbor distances testing the theoretical assumption of cascade interaction. Shown in Fig. 10 is a histogram of nearest neighbor distances, with 10,000 points from the PTRAC dataset considered. The average separation distance for this sample size is 56 um. Ten successive trials were conducted for different sets of points, with an average variance of 441 um, corresponding to a standard deviation of 21 um. The standard deviation is roughly 37% the magnitude of the average,

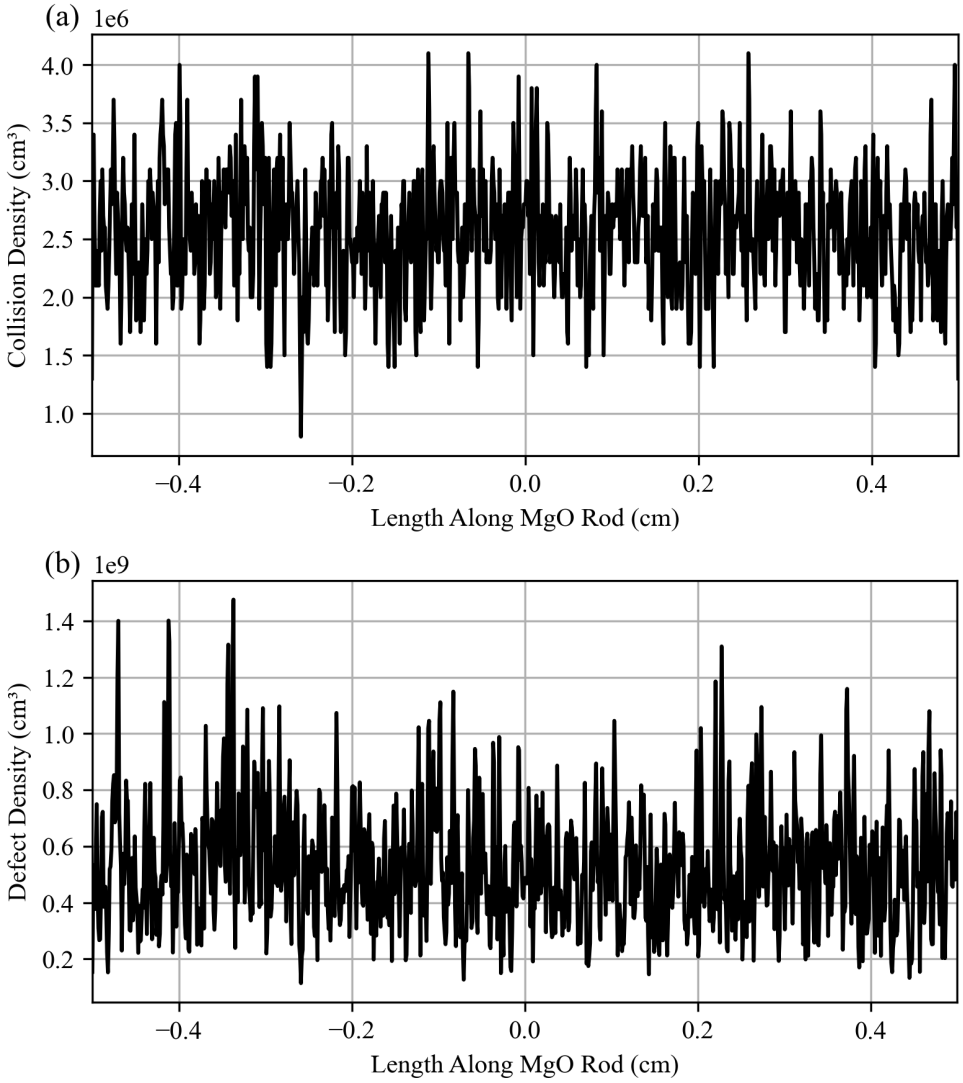

Figure 9: Collision (a) and defect (b) density plots along the x-axis of the MgO sample simulated in MCNP. Density fluctuations resemble random noise, and are qualitatively identical along the other spatial axes.

indicating a wide spread in the nearest neighbor distance.

As discussed in Sec. 3.4.4, 10,000 points were considered for this study. Computing nearest neighbor distance becomes exponentially more expensive with more data, so considering the full dataset was not possible. The 10,000 point computation took one hour and 57 minutes to complete on a single Intel® Core™ i7-10870H CPU running at 2.20 GHz. As will be discussed below, these results still serve effectively

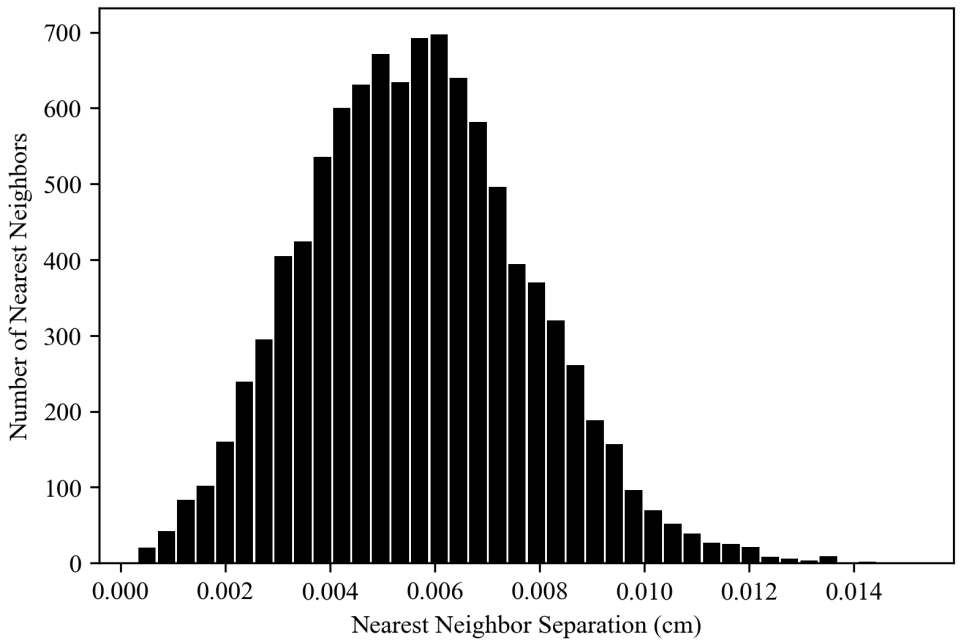

Figure 10: Histogram of the distances between nearest neighbors for a set of points taken from the PTRAC data. The average separation distance is 0.0056 cm with significant spread.

to characterize nearest neighbor distance for analysis, so the use of high performance computing resources to include more points was deemed unnecessary. The nearest neighbor distance scales with the cube root of the density of points in the volume - even with high performance computing resources, it is infeasible to directly compute this distance for relevant doses. Using the number of collisions and the normalized integrated flux from the f4 tally, the nearest neighbor distances for 10,000 points were scaled to the dose range of interest. Shown in Tab. 3 are the scaled nearest neighbor distances for relevant neutron doses. The forbidden volume, $9a_0$, with a lattice constant equal to 4.26 Å, is equal to 3.7 nm [13, 34]. At 3×10^{16} n/cm^2, the separation distance between PKA events is 21.5 nm, or $5.6 \times 9a_0$. While the length scales of collision cascades for varying energy are not accounted for, the production of multiple lasting defects in a cascade implies they are at least larger than a single forbidden volume, and would often be several times larger; furthermore, the

probability distribution of nearest neighbor distances is wide, with many PKA events having considerably shorter separation distances than the average. It is therefore not unreasonable to expect defect cascade overlap begins to appear near doses of 3×10^{16} n/cm^2, and becomes more pronounced as dose increases. By a dose of 10^{19} n/cm^2, the separation distance of PKA events is less than twice the radius of the forbidden volume, suggesting that most defects produced across the sample are annihilating, and collision cascades are producing fewer defects on average, in keeping with saturation theory.

Table 3: Average distance between PKA sites for varying experimentally relevant doses. The radius within which recombination is expected to occur instantly is 3.7 nm [13].

Neutron Dose (n/cm^2)	Nearest Neighbor Distance (nm)
10^{14}	285.6
10^{15}	132.5
10^{16}	61.5
10^{17}	28.6
10^{18}	13.3
10^{19}	6.2

4.3 Annealing Behavior

Also a prominent potential source of disagreement is the difference in annealing conditions between the experimental and computational results. As previously discussed, the experiments were conducted in a reactor over a range of one to tens of hours [11, 12]. When removed from the reactor environment, extreme care to prevent optical bleaching and temperature changes was not taken. This introduces myriad complications in comparing the two samples, and none of these complications can be corrected for within the scope of this work due to lack of documentation. This limits the granularity one can achieve from an annealing investigation, but at least some intuition may be applied from earlier discussions. Referring again to the results by

Uberuaga et al., the number of defects existing in the material following irradiation is heavily time-dependent [19–21]. Following a particular collision cascade, the total number of defects in the material peaks within the first tens of femtoseconds, and drops to a relative plateau by around ten picoseconds. Much later, on the order of hours, the experimental results show that a small amount of further annealing has occurred.

A straightforward model for this behavior is an exponential fit in log scale. Two example results of this fit are shown in Fig. 11. These fits compare the defect concentration at a particular dose over varying time, defined by three points:

- The total displacement count from Uberuaga et al.
- The number of "lasting defects" from the computation
- The experimental result

The first fit is to a dose within the region of strong agreement between computation and experiment, while the second fit is taken from the region of worst disagreement. In the low dose regime, it is indicated that the vast majority of annealing is undergone in the first 10 ps, with the defect concentration stabilizing long before experimental time scales are reached. Conversely, for middling to high dose, it is suggested that substantially more annealing occurs between the end of the cluster dynamics data and the experimental measurements. This would further indicate that defect saturation plays a larger role at high dose than is predicted by the model.

Implied in these fits is the assumption that the underlying computational model accounts for all dominant physical processes. The model does not possess a complete physical accounting of processes for defect saturation. Any characterization of the time scales over which post-collisional saturation effects cause further annealing is thus incomplete. This not only means that the relative placement of the "lasting

defects" prediction is off, but also potentially smears out the annealing curve for defect-saturated materials. A further contributing factor to this issue is the neutron flux in the HFIR HTS - as mentioned before, the total neutron flux is 5×10^{15} n/cm^2-s. With this flux, over the 10 ps window where most of the annealing occurs, a dose of only 5×10^4 n/cm^2 is undertaken by the material. To achieve even the lower dose of the two fits shown, the duration of the sample's irradiation will be on the order of tens to hundreds of seconds. For larger doses, several hours are needed. This relaxes the core assumption in these fits that the entire dose is deposited at once, implying that over time, defect cascades will be introduced to the system in isolation from each other due to the very short time scale of the ballistic phase. If modeled with the temporal effects of experiment, a log-log plot of defect concentration across time scales should show steady linear growth, then taper off with saturation, matching closely to the main results plot; this tracks with reporting in the literature, as total dose is time dependent [11, 12]. Considering this, a coarse analysis of time dependence offers a suggestion of the mathematical formulation of combined defect annealing behavior. An accurate assessment of annealing behavior and its time dependence would require a more thorough representation of experimental conditions and reactor environment, along with a deeper understanding of defect cascade annealing and saturation effects. Regardless, the presented analysis provides some insight: the vast majority of defect annealing, following a collision cascade, occurs within the first 10 ps. Exactly what this fraction is cannot be determined, but taking the strong agreement at low dose as accurate, the fraction outweighs annealing which occurs at larger time scales. It may then be inferred that the optical bleaching and handling of the samples post-irradiation did not strongly affect on the defect concentration in the samples.

$$F(t) = 10^{ae^{bx}+c} \tag{14}$$

The method used to produce the fits must also be addressed. Initially, attempts were made to fit an exponential curve directly to the data, however these attempts were unsuccessful. The relationship between the points in the plots only appears exponential in a log-log scale. Fitting attempts were successful after the data were log-scaled, however this produces fits of the form: $10^{ae^{bx}}$, an functional form which does not have a physical analog. This further supports the notion that annealing behavior does not adhere to a simple exponential relationship, but perhaps is represented by multiple annihilation processes. There is insufficient data to test whether this is the case, however further investigation is warranted.

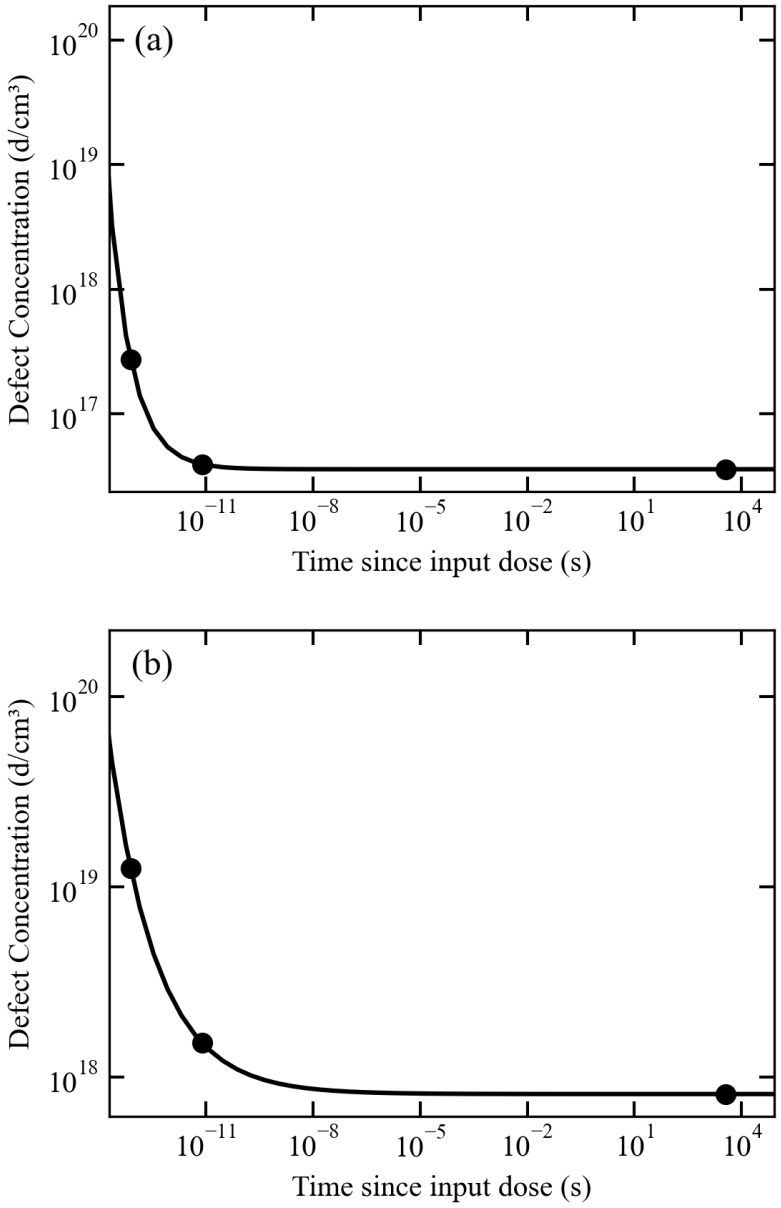

Figure 11: Exponential fits to the number of defects predicted or measured in the MgO sample across time scales. These plots showcase multiple complications with a direct time scale analysis. The doses of each plot - 3.6×10^{16} (a) and 8.1×10^{17} n/cm^2 (b) - showcase the differences examining the regions of strong agreement vs strong disagreement between the experiments and the computation. For low dose, the vast majority of annealing appears to occur within 10 ps, while for high dose, a significant fraction appears to occur over larger time scales.

4.4 Collisional Analysis

4.4.1 Initial investigation

Further investigation was also carried out into the energy distribution of collisions and PKA's produced by MCNP from the HFIR spectrum. This investigation unearthed several peculiarities rooted in MCNP's limitations and its handling of neutron transport, which would otherwise have gone unnoticed. The collisional behavior was first analyzed using a scatter plot of all incoming neutron energies and their corresponding deposited energies. Shown in Fig. 12, the expected relationship of kinetic energy deposition from elastic scattering can be seen in the smooth linearity of the region above 10 eV incoming energy. The maximum transferable energy increases linearly with energy available in the system. In the regime of high incident energy, a few scatters can be seen which break this rule - these are the inelastic scatter events which were touched on in Ch. III, and are discussed in detail further below. Additionally, in the low energy regime, the elastic scatter relationship exhibits peculiar behavior. This is most likely explained by thermal effects, where the energy in the target relative to the incident neutron is not negligibly small. In some extreme cases, neutron upscattering occurs in this regime. The energy range of these effects renders them irrelevant, so they may be safely ignored. Finally, horizontal lines can be observed all along the spectrum. These lines suggest that several incident neutrons of different energies have deposited exactly the same energy upon collision. The reason this occurs is unclear. Whatever the reason, close inspection of the data reveals that there are very few of these anomalies relative to total collisions, and further that they only occur for relatively low energy deposition. These are therefore also safe to ignore.

Fig. 13 emphasizes additional features of the energy deposition scatterplot with two additional graphics. Plot (a) is a reproduction of Fig. 12 with dot size scaled

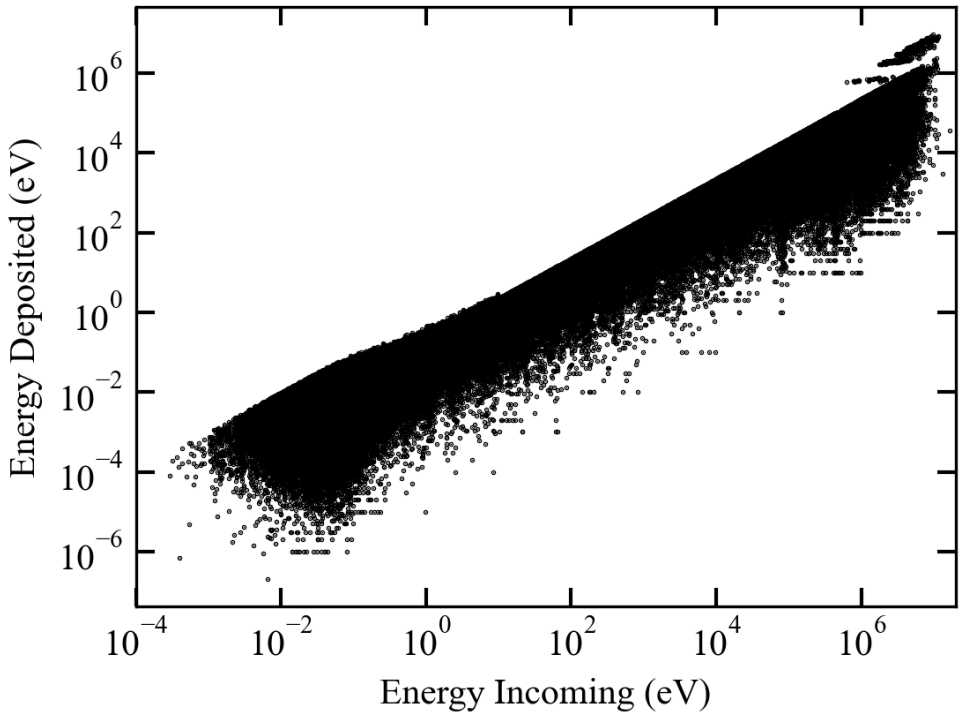

Figure 12: Scatter plot of incident neutron energies and corresponding deposited energies. Several characteristics may be observed, including inelastic scatter in the high energy regime, thermal effects in the low energy regime, and suspicious horizontal lines for low energy deposition across all incident energies.

down by a factor of 10^4, serving as an effective heat map of collision frequency. As expected, the majority of observed collisions are seen at the low and high ends of the spectrum. This follows as expected with the probability distribution of the HFIR spectrum. At high energy, the resonances in the O and Mg cross-sections can be observed. Unexpected, however, are the abrupt vertical lines across the mid-range of incident energies. These lines suggest that at intervals, the overall likelihood of collision occurrence abruptly drops. Furthermore, the likelihood of occurrence appears to increase with energy across each of these regions. The most likely possible explanation for this phenomenon is the piece-wise nature of the provided HFIR spectrum. As the measured energy spectrum was not continuous with energy, MCNP could only be provided the "blocky" spectrum given in Fig. 2. Across a given energy bin, MCNP

samples uniformly. Across a wide range of energies, this results in several chunks of equiprobable energies which are not inter-continuous. This is an unavoidable outcome which would arise in any application of the measured reactor spectrum. Due to the indirect nature of neutron detection, it is infeasible to obtain a fully continuous measurement of a reactor neutron spectrum [59].

4.4.2 Inelastic Scattering

Shown in Fig. 13 (b) is a closeup of the inelastic scatter region, highlighted in the top right of plot (a). (b) includes a red line indicating the maximum transferable energy by elastic scattering. From the overall plot, the relative occurrence of inelastic scatters is quite low; however, these events may not be ignored due to their relatively high energy deposition. As mentioned in Sec. 3.4.2, the first three nuclear excited states are accounted for in the code. These correspond to all energy transfers which fall below the maximum elastically transferable energy plus 1.38 MeV, the first excited state of Mg-24 [58]. As seen in Fig. 13, however, this only accounts for a fraction of the inelastic scatters observed. Nuclear excited states are not well characterized for many nuclides, especially for those without appreciable applications in nuclear engineering. Nuclides of O and Mg, are not among the best characterized, and while data exist on observed excited states, they are often unclear, and hundreds or thousands of excited states are reported to exist [58]. These excited states become more densely packed and worse characterized as energy increases [60]. While this alone does not warrant discarding these collisions, considerably more important are the cross-sections for these interactions occurring. Many excited states have only been experimentally verified a handful of times, and as a result the existing cross-section data are extremely poor [60]. It is important to consider that MCNP can only predict these interactions based on provided cross-section data, and that these collision events come directly

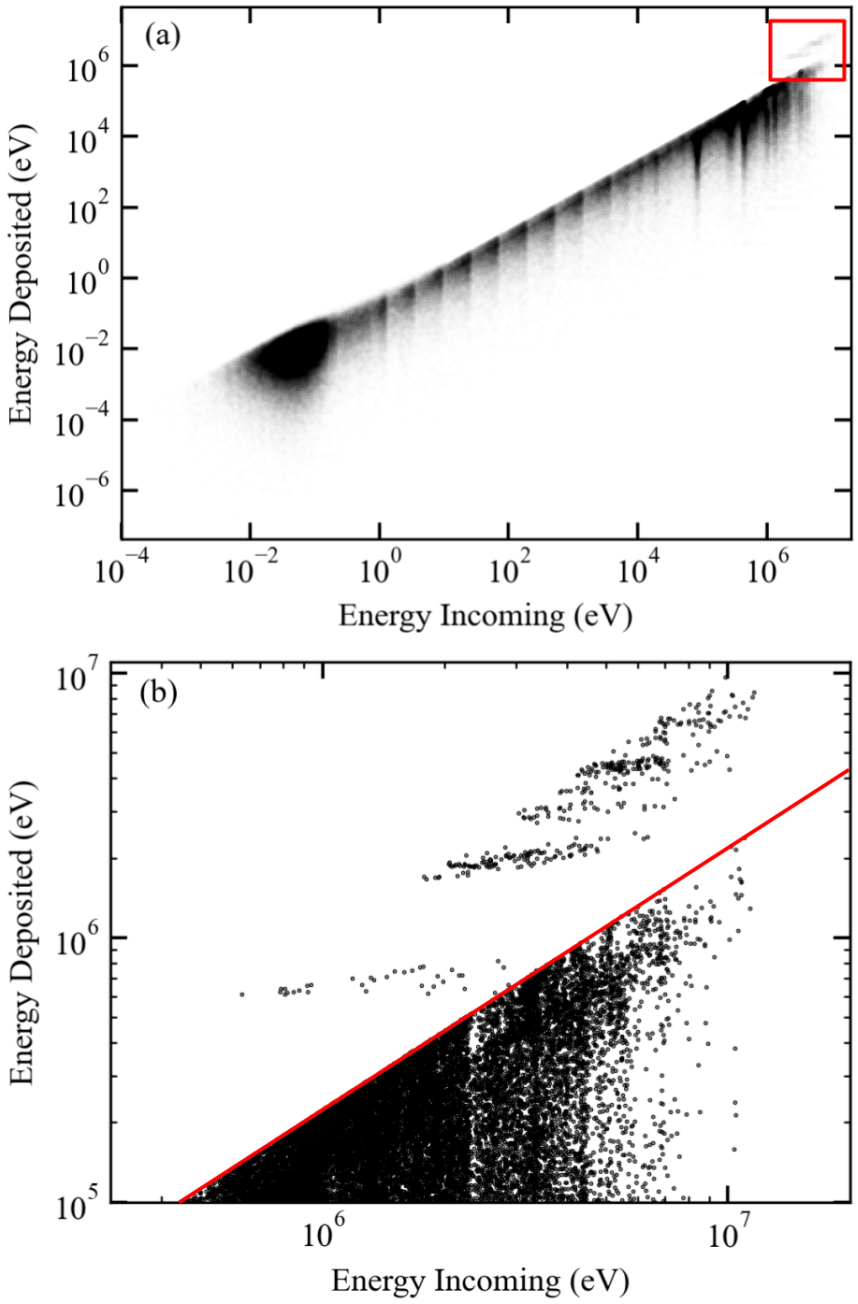

Figure 13: Scatter plot of incident neutron energies from the HFIR spectrum in MCNP and corresponding deposited energies with reduced dot size, along with closeup of the inelastic scatter region, indicated by the red square in part (a). Regions of high collision frequency stand out: resonances can be seen in the high energy regime, and the piece-wise nature of the input spectrum appears in the form of vertical cutoffs.

from these poor cross-section data. While it is reasonable to assume the lowest energy excited states have been characterized reasonably well, as energy increases the the inelastic scatter events give the appearance of occurring on a continuous spectrum. This is a limitation which severely inhibits accurate neutron transport simulations of any kind in the high energy regime. The problematic nature of this continuous appearance was compounded by an inability to parse specific excitation energies from the PTRAC output. The first three levels were clearly distinct from one another and could be manually corrected, however the blending together of higher energy scatters made the excitation energies indistinguishable from an energy transfer perspective. These complications resulted in the decision to discard inelastic scatters above the lowest three states. The exclusion of these uncorrected-for events appears to change the overall defect total by 0.9%, so for the HFIR spectrum, this limitation does not egregiously impact the results.

4.4.3 Collision Histograms

Collision frequency by energy was also modeled directly using a histogram. Shown in Fig. 14 are two histograms, showing number of collisions and defects produced by energy as they relate to incident and deposited energy. The first histogram, depicting number of collisions, provides an additional perspective on some of the properties discussed above from the scatter plots. Interestingly, the incident energy line showcases the energy bin cutoffs quite clearly, while their effects do not seem to manifest in deposited energy nearly as much. Additionally, the resonances can again be seen in the energies of the neutrons on collision, however the actual deposited energy severely mutes their presence. These are both likely results of the stochastic nature of energy deposition, which can be expected to have a smoothing effect on any jagged features in the incident spectrum. Finally, the inelastic scatter events can be seen at the up-

per end of the deposited energy histogram, bridging the gap between incident and deposited energy which normally results from elastic scattering. Again it is notable that these events comprise few counts overall. This figure matches closely to Fig. 2, indicating that the MCNP deck is running as expected.

The second histogram characterizes the reactor spectrum in terms of defects produced, plotting the number of collisions by incident energy against the number of defects produced by deposited energy, omitting all collisions which produce no defects. This figure builds intuition on how defect production depends on energy and provides insight into what can be expected from other spectra based on their energy distributions. The energy cutoff below which defect production cannot occur is clearly represented. Moreover, the linear energy dependence of defects produced is also evident. Based on both histograms, the deposited energy consistently lags below the incident energy - this is an expected result from the hard sphere collision model used with elastic scattering. This along with the expected energy dependence suggests that the plateauing of defects produced by deposited energy near 1 MeV is not solely the result of this displacement. Based on the theoretical models, this plateau behavior is likely the ionization limit L_C taking effect, which weakens the growth of defects produced by energy once it is exceeded. This suggests that for neutron sources with higher energies, the ionization limit should be expected to play a large role in effectively characterizing damage.

4.4.4 Interstitial Collision Tendency

The analyses above lead into yet another potential contributor to the deviations between the models and experiment for larger neutron doses. As dose and overall damage increase, the displacements created in the lattice lead to large numbers of trapped interstitials across the sample. Statistically, as the concentration of inter-

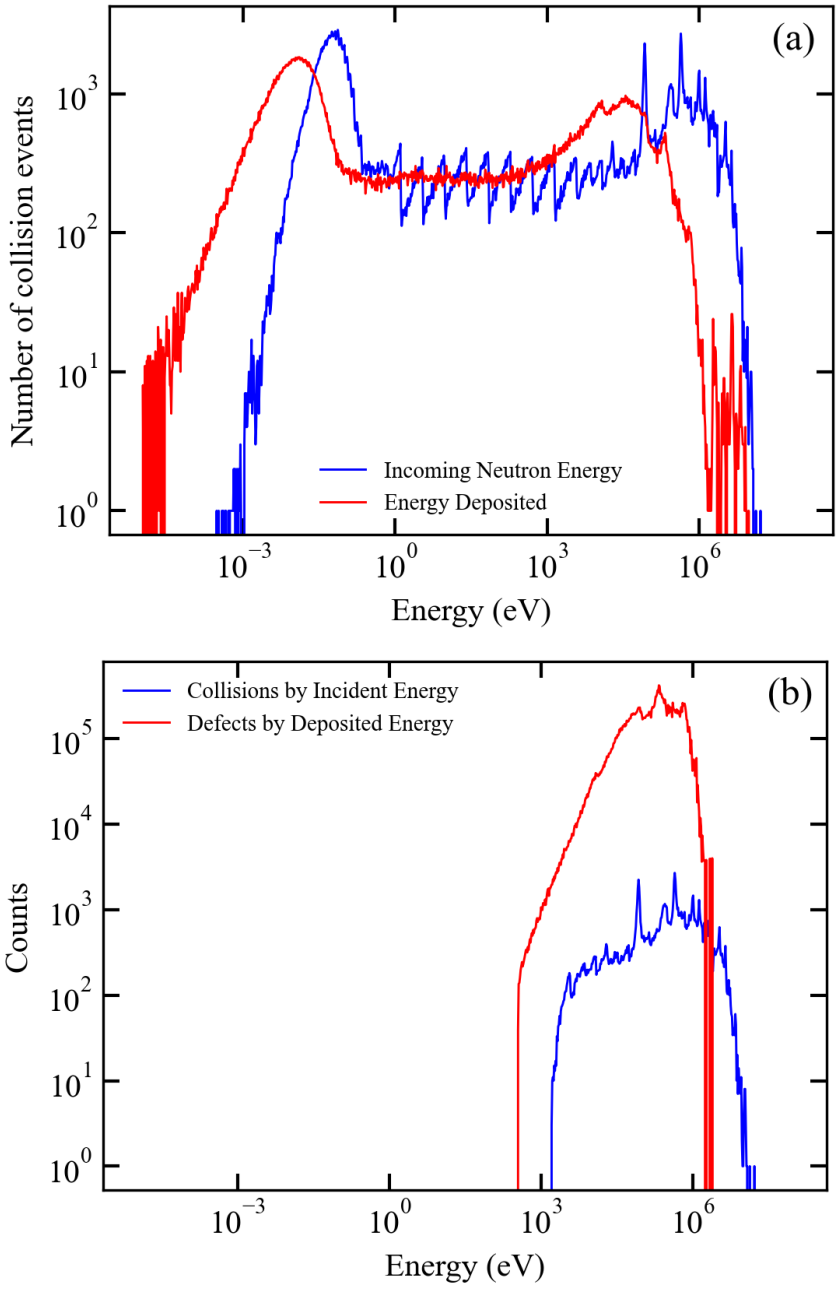

Figure 14: Histograms of number of collisions (a) and defects produced (b) by energy, comparing incident energy to energy deposited. Plot (a) showcases the energy bin cutoffs, resonances, and inelastic scatter events discussed previously, and otherwise matches well with Fig. 2. (b) is a histogram comparing neutron collisions by incident energy to defects produced by deposited energy. Only defect-producing collisions are included.

stitials increases, it is likely that some small number of neutron scatters will occur between an incident neutron and an interstitial, rather than a lattice ion. Theory and computational models do not provide strong insight into behavior of interstitial PKA's and the characteristics of their collision cascades, however it can reasonably be expected that a high energy interstitial PKA will behave similarly to a normal one. However, Uberuaga et al. report the diffusion barriers for isolated interstitials in MgO at 0.40 eV for O and 0.32 eV for Mg [19]. This considerably lower barrier to movement compared to the displacement energies of O and Mg ions from the lattice indicates that interstitials may be lifted over the diffusion barrier by neutron energy transfers much lower than those required to generate defects. Based on the separation distances provided in Tab. 3, it is reasonable that for doses $> 3\times10^{16}$ and high enough dose rates, collision cascades may be close enough together for neutron-stimulated interstitial diffusion to contribute appreciably to overall defect annealing. An order of magnitude analysis was carried out to determine whether or not this was feasible. Interaction cross-sections being the same, the likelihood of a neutron colliding with an interstitial over a lattice ion depends on the fractional presence of existing interstitials. If the number of interstitials is assumed to be equal to the number of vacancies, then one would expect, even at saturation, for the ratio of interstitials to lattice ions to be on the order of 1:1000 or less. For a dose of 10^{19} n/cm^2, using the surface area of the sample and generalizing the ratio of particles seen by the sample to collisions in the sample reported by PTRAC for fewer histories, approximately 4.2×10^{16} neutron collisions are expected to occur. Of these, only 4.2×10^{13} would then be expected to occur with interstitials. Even assuming every interstitial collision produces a 1:1 recombination, this number is far too low to produce an appreciable impact on the overall defect concentration. For lower doses, this number can be expected to decrease rapidly, as the ratio of interstitials to lattice ions decreases according to defect

concentration. This indicates that interstitial collisions should not be considered a substantial source of annealing.

4.5 TDE Comparison

The results of the investigation into average TDE predicted by the KP model versus NRT are presented in Fig. 15. As discussed across Sec. 2.5 and Sec. 3.4.2, the selection of an average TDE over two separate TDE's for Mg and O was required. An average TDE of 66 eV is found from equating the KP equations to the line developed off of the cluster dynamics results and solving for E_d. This produces quite strong agreement with the predictions discussed in Sec. 2.5, but an unanswered question remains as to whether the newer NRT model produces a more accurate result. Using the same method, an alternative average TDE value of 105 eV is determined. Based only on the various experimental measurements and simulation predictions of TDE's in MgO, 105 eV does not agree nearly as well with what would be expected to be the average. Further comparison is drawn in Fig. 15, which showcases the difference produced by these values. In orange is the saturation-free prediction made by the cluster dynamics results combined with the KP equations for the TDE value of 66 eV, while in teal is what NRT would predict using the same value. Substituting the KP value of 66 eV into the NRT model over-predicts the F-center defect concentration by a factor of 2.1. This value also predicts the onset of saturation from the HFIR to occur for doses of $> 6 \times 10^{18}$ n/cm^2 and energy deposition distances of < 7.29 nm, a value 1.9 times larger than the forbidden volume radius [13, 57]. This onset of saturation occurs well below what is expected from the formulated forbidden volume and saturation limit for MgO. Alternatively, the inverse occurs if the TDE determined from NRT is applied to the KP model - the F-center concentration is under-predicted by a factor of 2.1, and suggests that saturation occurs for doses of $> 1.4 \times 10^{19}$ n/cm^2

and distances of < 5.5 nm which is 1.4 greater than the accepted forbidden volume radius. An $E_d = 105$ eV is near twice the experimental measurements for either Mg or O and more than 10% higher than most computational values, and this provides further support for the choice of the KP model over NRT [7, 9, 18–21, 49–51].

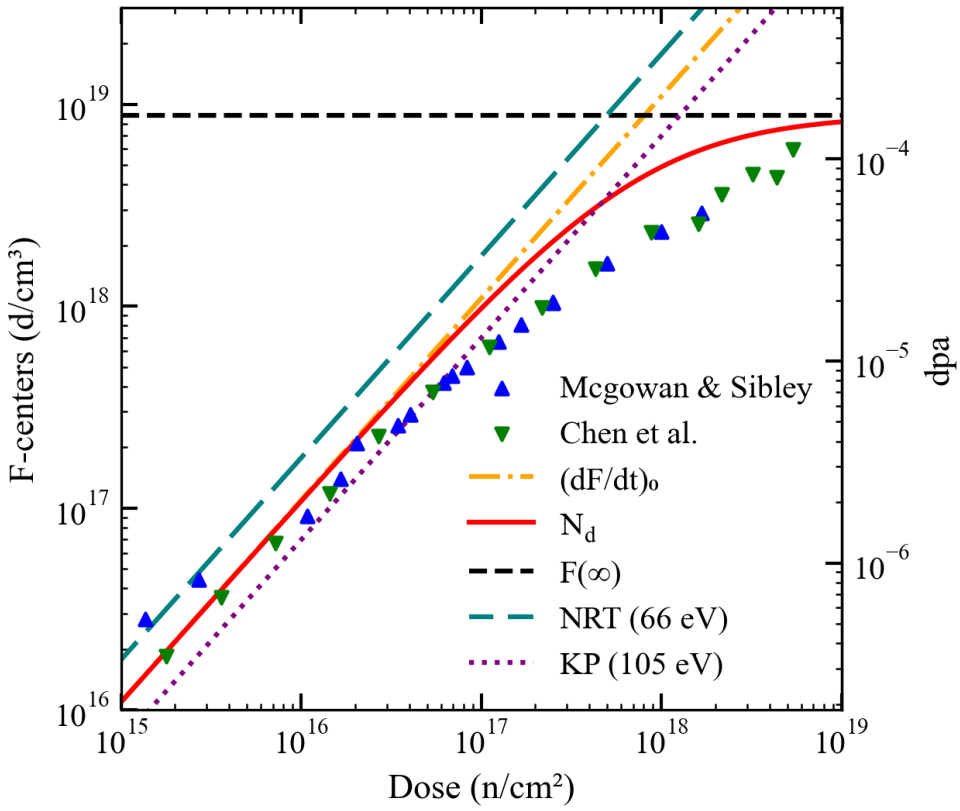

Figure 15: Modified plot of the overall sim results including a comparison with the TDE predicted by the NRT model.

4.6 Other Spectra

In the interest of generalizing the applicability of this model, three additional spectra have been applied, and their outputs are compared in Fig. 16. This investigation served to explore whether changing the input spectrum for the model produced results in line with expectations, or whether any strange behavior could be identified. The spectra investigated are a prompt U-235 fission spectrum, a 14.1 MeV D-T fusion source resembling the National Ignition Facility (NIF), and a 2.45 MeV D-D fusion source to resemble AFIT's neutron source in the Extreme Light Laboratory. Each source will be discussed in its own respective subsection. Overall, each of these sources appears to produce many more defects in the target than the HFIR spectrum, with the D-D source producing the fewest of the alternatives, and prompt fission source producing slightly fewer than the D-T source. This result is to be expected, considering relatively few neutrons sampled from the HFIR spectrum are capable of producing defects at all, while these spectra consist almost entirely of MeV range neutrons.

4.6.1 D-T Source

The D-T source, nearly replicating the neutron spectrum produced by the NIF, along with the other two spectra additional spectra, showcases a critical shortcoming within this model and the literature at large. The D-T source was the first of the three spectra to be investigated, and consists of a single line source of 14.1 MeV neutrons. This achieves the highest defect production of all the sources plotted, but considering the overwhelmingly high energies of these neutrons compared to those of the HFIR, one would expect the damage predictions to be even higher. As it stands, the D-T source produces roughly seven times the defects of the HFIR spectrum using this model for an identical neutron dose. It should produce substantially more, however inelastic scattering accounts for nearly half the recorded collisions and must be

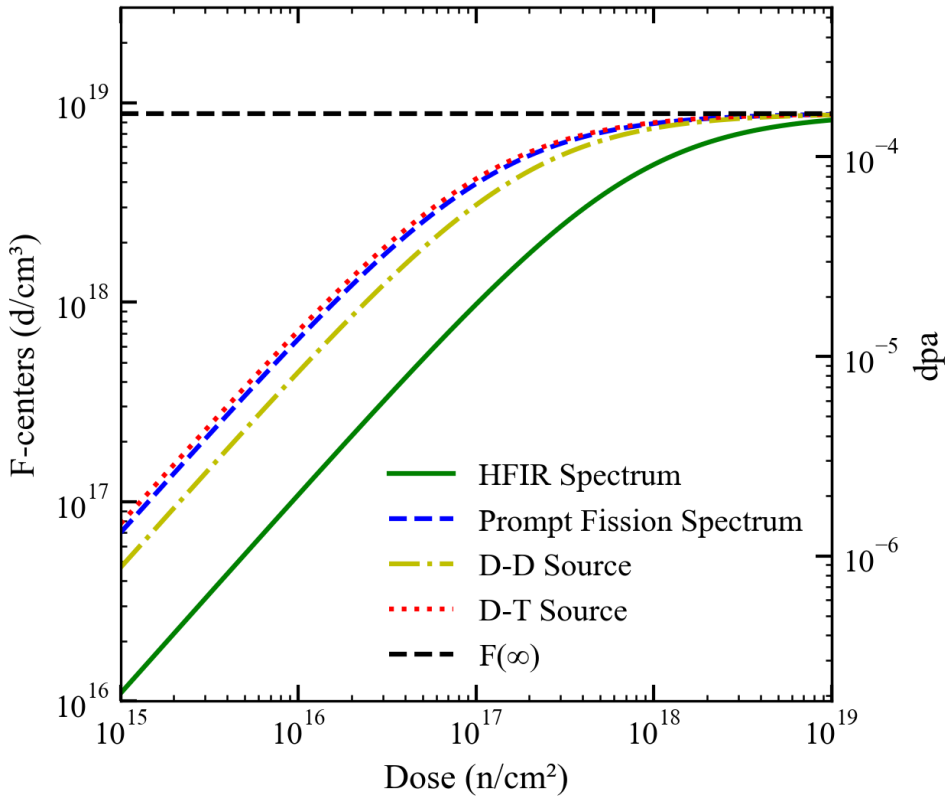

Figure 16: Comparison of HFIR results to other neutron sources, including the U-235 prompt fission spectrum, a D-T fusion source, and a D-D fusion source. All compared sources produce more defects, though this is expected considering the energy distribution of the HFIR spectrum is relatively low.

discarded for reasons discussed in Sec. 4.4.2. As discussed previously, when using the HFIR spectrum, the number of collisions which must be discarded is an insignificant number. Compared to the total number of collisions recorded, on average 0.06% of them are discarded. In the case of the D-T spectrum, on the other hand, 41.1% of collisions are inelastic scatters that are too energetic to be handled. The other spectra also exemplify this issue to a lesser extent. The problem with accounting for all of these inelastic scatters in the post-processing code, as discussed above, is that excited nuclear states are not well studied. Inherently, the study of excited nuclear states is extremely difficult, because as neutron energy increases into the

MeV range and beyond, the number of nuclear excited states increases exponentially until it appears continuous [58]. This is a very important problem when considering any computational model involving high energy neutron radiation, because due to the overwhelming lack of corroborating cross-sectional data, model validation is extremely difficult in this regime.

4.6.2 Prompt Fission Spectrum

The prompt fission spectrum of U-235 is particularly interesting to compare against the HFIR spectrum. The wide difference in defect production between the two highlights how much moderation occurs in the HFIR to result in a neutron spectrum where only around 25% of neutrons are energetic enough to produce defects. The fission spectrum used is the common calculated Watt fission spectrum, and is shown in Fig. 17. The numbers of neutron scatters across a spectrum of energies are plotted and fit with a line. Based on this spectrum, near all prompt fission neutrons are energetic enough to produce defects, so a side by side comparison of equal dose from each spectrum should be expected to be different. Interestingly, this spectrum also produces more defects than the D-D source, which is represented as a line source of 2.45 MeV neutrons. The prompt fission spectrum peaks at around 1 MeV, but with a long tail of high energy neutrons extending above 10 MeV. This may make it a more energetic source overall than the D-D source, however it is alternatively possible that inelastic scattering makes the D-D source appear low. It is difficult to compare the prompt spectrum results to the D-T source, however this time the results are not nearly as heavily impacted by the inelastic scattering. In this case, only 0.8% of collisions were discarded, making this result relatively reliable. This additionally provides a point of reference for the expectation of the D-T prediction. The difference between 0.8% and 41.1% indicates that the D-T spectrum should produce near

double the damage it currently shows, at minimum.

4.6.3 D-D Source

Finally, a D-D fusion source was investigated for its relevance to AFIT, and to better understand the cutoff at which inelastic scattering impacts results. The D-D source is the least energetic overall of the additional sources. Interestingly, however, in this case the percentage of results discarded is 1.5%, almost double that of the prompt fission spectrum. This highlights that from the prompt spectrum, a large number of collisions are relatively low energy neutrons which are less prone to inelastic scatter, while the 2.45 MeV neutrons from the D-D source are all high enough energy for inelastic scatter to be a concern. Although significant, the 1.5% inaccuracy of D-D fusion neutrons provides a useful statistical comparison between the continuum source of prompt fission neutrons and the higher energy line source neutrons of D-T reactions. In this regime, a correction factor could potentially be determined, broadening the uncertainty on the model's result while preserving its utility as a surveying tool.

The investigation of these three spectra has produced encouraging results. While the D-T source proved far too energetic for the model to handle, the prompt fission spectrum and D-D source each showed to be relatively unaffected by the inelastic scatter cutoff in the post-processing code. This investigation provides confidence in the behavior of the model for alternative neutron spectra, and has served to characterize the impact of inelastic scattering on the validity of any results. The logical next step in determining this model's utility is acquiring experimental data to compare against the two spectra which are not substantially impacted. Of course, inelastic scattering is not the only element of the model which might produce inaccuracy; the behavior of high energy PKA's in collision cascades as a whole is not as well characterized as those produced from keV-order neutrons. The generalization of cluster dynamics data

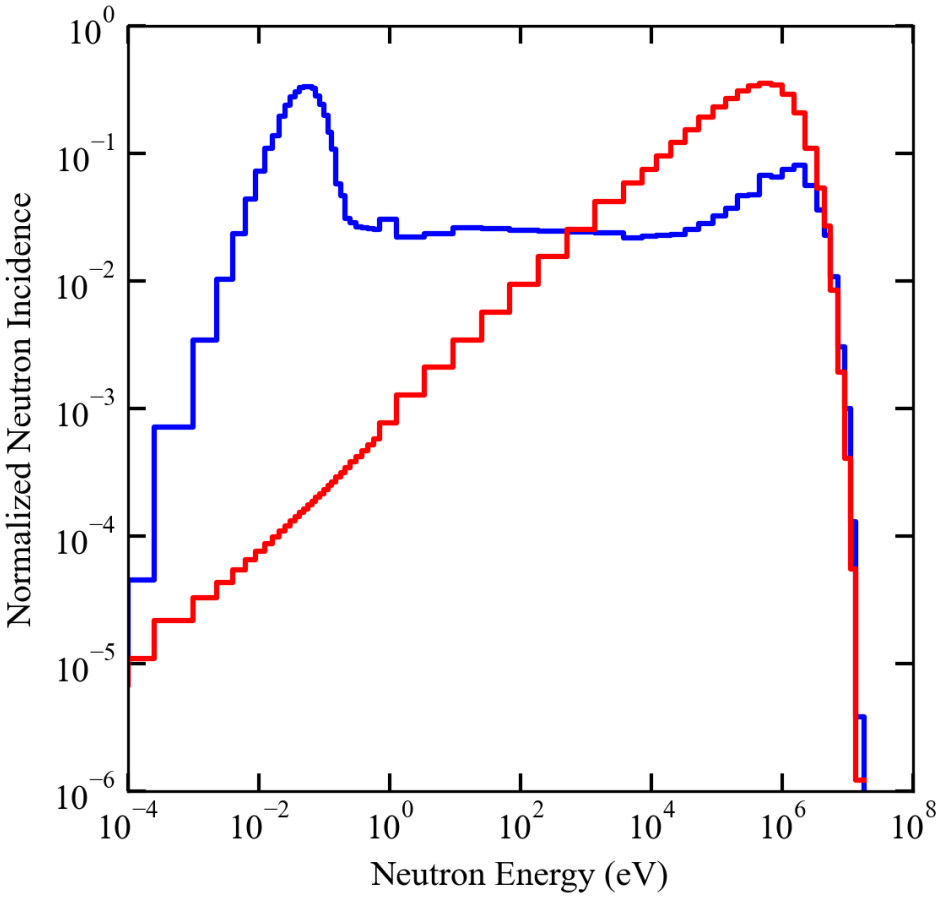

Figure 17: Overlay comparing the normalized HFIR spectrum to the normalized U-235 calculated prompt fission spectrum. The Watt fission spectrum was projected against identical energy bins to the HFIR spectrum for consistency. The prompt fission spectrum consists primarily of high neutron energies by comparison, and as a result produces more defects for equivalent dose.

from keV into the MeV range using older theory leaves open questions on the spatial extent of defect cascades and the role of excited nuclear states in cascade formation and propagation.

V. Conclusions

5.1 Summary

The study of radiation-induced defect production in a material and subsequent defect evolution is broad, multifaceted, and extremely difficult. Computational and experimental researchers have worked to characterize the behavior of radiation-induced material defects for almost a century, and no comprehensive tool or model yet exists to handle the problem. This is largely due to the multiscale nature of the phenomena at play, with collision cascades and initial annealing of defects predicted to occur on the order of picoseconds while the earliest experimental data are recorded as early as seconds after irradiation has occurred. Computational efforts to investigate defect evolution are often limited either by time scale, size, or range of incident neutron energies, with no model yet developed able to completely replicate an experimental setup. Experiments, along with many desired applications of various devices, are subjected to sweeping spectra of incident radiation, do not exist in a vacuum isolated from the rest of the world, and are concerned with large time scale effects. As technology and manufacturing techniques advance, the importance of understanding radiation effects on newer, smaller, more delicate devices grows. Neither the existing experimental techniques nor computational models currently available are suitably fast and inexpensive to keep pace with rapid advancements of device evolution.

The goal of this research was to develop a fast model capable of surveying F-center production in MgO crystal for varying doses and producing results consistent with experiments. This model used MCNP to handle neutron transport through a MgO rod matching the conditions of the experiments, employed defect production theory by Kinchin and Pease along with atomistic simulation results from Uberuaga et al. to predict the production of defects in the target crystal, and finally applied defect

saturation theory to produce a relationship between F-center concentration and neutron dose compared against the experimental data. The model produced results in strong agreement with experimental data for doses $< 3 \times 10^{16}$, while disagreeing for larger doses by a factor as high as 2.2. Several potential explanations for disagreement between the model and experiments were investigated, including poor accounting for the sizes and potential interaction of collision cascades, wide fluctuation in nearest neighbor distance, no consideration for annealing between 10 ps and long term, peculiarities in the conditions of the simulation, and neutron collisions with interstitials. Of these, the most promising are the dimensions of the collision cascades and accounting for the fluctuations in nearest neighbor distance. The temporal analysis indicated that for doses below 3×10^{16} n/cm^2, annealing is minimal after the first 10 ps. Investigating the collision profile output from PTRAC highlighted several inaccuracies including the handling of inelastic scattering, the saw-tooth representation of the input spectrum, and machine precision. Of these, only the input spectrum could feasibly affect the results, however it could not be accounted for more accurately.

Also discussed was the choice of the TDE, as well as comparisons made between the HFIR results and those of a prompt U-235 fission source, a D-T fusion source, and a D-D fusion source. The TDE predicted using the KP formulation was compared against that of NRT and it was determined that prediction made using KP was more accurate. This supports the decision to use the KP formulation over NRT in the model. From the additional spectra investigation, the important conclusion was drawn that high energy neutron damage is inherently problematic to predict. The D-T fusion source could not be adequately investigated due to 41.1% of collisions needing to be discarded due to being high energy inelastic scatter events. Inelastic scattering is poorly understood and lacking detailed cross-section data. The prompt fission spectrum and D-D source were observed to be less impacted by inelastic scattering,

with the potential for a correction factor to be used without compromising usability.

This work primarily contributed the following to the academic community:

- Accurate, inexpensive prediction of defect concentration in a material resulting from neutron irradiation in a realistic experimental environment.
- Proof of concept for development of a fast computational model capable of surveying radiation damage based on existing research and tools.
- Evidence to support the validity of MCNP, the continuum approach, and cross-section data in the sub-mean free path regime.
- Exploration of factors contributing to inaccuracy between computations of defect evolution and experimental measurements.

5.2 Limitations

Inherently, tackling a problem as multifaceted and multiscale as predicting long term atomic radiation damage within this work's scope requires extensive simplification. This model combines results, techniques, and products from several different fields, and cannot incorporate the entire scope of each study. From an experimental perspective, the model only considers the results of two experiments for a single spectrum. From a cluster dynamics perspective, the microscopic detail of this model tracking individual ion movement is not present. A continuum approach is used rather than crystal structure, defect cascades, interactions with surrounding nuclei, clustering, and mobility are neglected, and grain boundaries and impurities are assumed to be absent. All of these assumptions were made deliberately, with the intent to avoid concepts used in cluster dynamics which have never been validated through experimental measurement, and to gauge the relative importance of concepts such as defect clustering in producing accurate long term estimates. Nevertheless, this lack of

detail must be acknowledged as a shortcoming compared to existing cluster dynamics studies.

Many broad statements can be made regarding the validity if this model and its portability to other materials. All quantities relevant to the final prediction are specific to MgO, including the experimental data, cluster dynamics results, TDE values, interatomic separation, forbidden volume, and more. Expanding this model to another material would require extensive study of that material and an overhaul of the data in the existing framework. The accuracy of the model when generalized to other materials has yet to be validated. Fundamentally, this model and the comparisons made in this work serve as a proof of concept.

5.3 Future Work

Several additional investigations are warranted following this work. The model produced indicates strong potential for wide application and surveying of materials. There is ample room for improvement in this application. Most pressing is investigation into the disagreements between the model and the experiments for doses $> 3 \times 10^{16}$ n/cm^2. Several paths forward exist in this respect, including:

- Investigate the observed disagreement between apparent slopes of the experimental data versus the model. A mathematical analysis exploring physical functional forms which accurately fit the experimental data, along with research into defect concentrations in materials subject to low or zero neutron dose, may highlight assumptions made regarding the linearity of F-center concentration with dose.

- Investigate overlap of collision cascades and the varying nearest neighbor distances of collision sites, and their effects on defect saturation as dose increases,

and methodically examining the role of dose rate. This has been identified as the most likely source of disagreement in the high dose region.

- Investigate annealing behavior observed either experimentally or computationally between the orders of picoseconds and seconds. The temporal analysis conducted here did not resolve the question of whether long term annealing is responsible for disagreement at high dose.

- Produce results for different spectra and geometries and compare against corresponding data to confirm the trends observed here. The present model has been developed from a limited data set. Using the D-D fusion source at AFIT, one could collect new data to compare against the prediction made in this paper.

- Investigate the appearance of linear regions in the experimental data used in this work. A preliminary analysis is provided in Appendix E, and a deeper study is recommended.

While refining the model for MgO should be the primary followup to this research, it is not the only matter warranting attention. Several further avenues of future work have become evident from this work, including the following:

- The model should be expanded to investigate other materials - particularly, materials with different bonding types and structures. It remains to be determined whether this model works for all materials, or only with ionic crystals, or only with MgO, among other possibilities.

- There exists no experimental data confirming computational predictions made of the ballistic phase following a neutron collision. Data exploring these time scales would be invaluable to the community, and could be achieved using modern technology with careful setup.

- MCNP 6.3 brings a more optimized and user friendly version of the PTRAC module to the table, as well as built in capability for parallelization of simulations. This should be integrated into this model and investigated for improvements in performance and efficiency.

Appendix A. Experimental Data

Neutron Dose (n/cm^2)	Defect Concentration (n/cm^3)
1.36E+15	2.81E+16
1.79E+15	1.84E+16
2.70E+15	4.44E+16
3.62E+15	3.60E+16
7.23E+15	6.71E+16
1.08E+16	9.13E+16
1.44E+16	1.18E+17
1.66E+16	1.39E+17
2.05E+16	2.09E+17
2.70E+16	2.27E+17
3.46E+16	2.56E+17
5.39E+16	3.74E+17
6.19E+16	4.19E+17
6.91E+16	4.51E+17
8.31E+16	4.99E+17
1.11E+17	6.26E+17
1.25E+17	6.70E+17
1.66E+17	8.11E+17
2.17E+17	9.87E+17
2.49E+17	1.04E+18
2.51E+17	1.05E+18
4.33E+17	1.51E+18
5.01E+17	1.63E+18
8.75E+17	2.31E+18
9.99E+17	2.33E+18
1.61E+18	2.56E+18
1.67E+18	2.90E+18
2.16E+18	3.58E+18
3.21E+18	4.49E+18
4.36E+18	4.34E+18
5.40E+18	5.98E+18

Appendix B. MCNP Input Deck

```
Plane isotropic 1-MeV neutron source in MgO prism
c ******************** BLOCK 1: CELL CARDS ***************************
10 1 -3.58 -10          imp:p=1  $ prism
20 0        10 -20      imp:p=1  $ kill neutrons outside prism
30 0        20          imp:p=0

c ******************** BLOCK 2: SURFACE CARDS ************************
10 rpp -0.5  0.5 -0.05  0.05 -0.05  0.05    $ MgO rod (larger 08312022)
20 so  0.51                                 $ Void edge

c ******************** BLOCK 3: DATA CARDS ***************************
SDEF sur=20 nrm=-1 par=n erg=d3 $ shell source emitting isotropically
SI3  0 1e-10 2.53e-10 1.01e-9 2.27e-9 4.04e-9 6.32e-9 9.09e-9 1.24e-8
     1.62e-8 2.05e-8 2.53e-8 3.06e-8 3.64e-8 4.27e-8 4.95e-8 5.68e-8
     6.51e-8 7.47e-8 8.6e-8 9.9e-8 1.14e-7 1.31e-7 1.52e-7 1.79e-7
     2.12e-7 2.54e-7 3.08e-7 3.75e-7 4.61e-7 5.69e-7 7.06e-7 1.265e-6
     3.45e-6 9.38e-6 2.55e-5 6.93e-5 1.88e-4 5.12e-4 1.39e-3 3.78e-3
     7.33e-3 1.21e-2 1.99e-2 3.28e-2 5.41e-2 8.92e-2 1.38e-1 2.07e-1
     3.08e-1 4.6e-1 6.86e-1 1.02 1.53 2.28 3.4 4.52 5.52 7.13 9.09
     1.11e1 1.36e1 1.823e1
SP3  0 7.04855e-06 2.74845e-05 0.000536624 0.00191833 0.00452698
     0.00844859 0.0133882 0.0195311 0.0257896 0.0290964 0.0372163
     0.04152 0.0443857 0.0454208 0.0450543 0.0430747 0.0424564
     0.0415663 0.037321 0.03194 0.0262508 0.0190009 0.0149288
     0.00869992 0.00731035 0.00511724 0.00507858 0.0047765 0.00488404
     0.0048937 0.00493861 0.013509 0.014125 0.0148084 0.0165564
     0.0162302 0.0159205 0.0156599 0.0152771 0.0151614 0.0105809
     0.00882806 0.00890654 0.00919654 0.00995174 0.0110978 0.0114984
     0.0124922 0.0154788 0.0156421 0.0222106 0.0213225 0.0249579
     0.0265831 0.0184954 0.00895447 0.00414857 0.00243823 0.000655233
     0.000182964 2.37637e-05 9.79043e-07
mode n                        $ track neutrons
rand seed=19073486328125      $ 19073486328125
nps 100000000                 $ number of histories to be run
print
ptrac file=asc write=all max=1000000000
f4:n 10
c MATERIAL 1: MAGNESIUM OXIDE
m1 12024 -.395 12025 -.05 12026 -.055 8016 -0.5  $ Magnesium Oxide
```

Appendix C. TDE Measurements

Table 4: Compilation of threshold displacement energies from various experimental and computational papers. In addition to these values, refer to Kittiratanawasin et al. for a computation of TDE's over a continuum of directions [51].

Nucleus	Displacement Energy (eV)	Crystallographic Direction	Reference
O			
Experiments	60	Unknown	[49]
	97	[0 0 2]	[7]
	44	[0 0 1]	[9]
	46	[1 1 1]	[9]
	64	[0 1 1]	[9]
Simulations	47.5	[1 2 1]	[18]
	67	[1 2 1], [1 3 1]	[50]
	73	[1 3 5]	[50]
	>150	[1 7 11]	[50]
	>65	Unknown	[19]
Mg			
Experiments	64	[0 0 2]	[7]
	60	[0 0 1], [0 1 1], [1 1 1]	[9]
Simulations	41.5	Average Value	[18]
	136	[1 0 0]	[50]
	153	[1 2 0]	[50]
	90	[1 3 1]	[50]
	>90	Unknown	[19]

Appendix D. Defect Total Poisson Analysis

The following analysis attempts to consider the impact of MCNP's statistical uncertainty on the final defect total using coefficients of variation. A few notes should be taken before reading:

- Predominantly, the error implicit in the number of defects predicted from each neutron collision was assumed to be 100% accurate.
- The error introduced to the assessment of neutron collisions by MCNP resulting from cross-section covariances was assumed to be zero.
- The validity of the coefficient of variation to describe a non-poisson distributed random variable is uncertain.
- Mean values were used to convert relative error to absolute error, when the quantity of interest was not a mean, but a total.
- The final step of summing the weighted errors should have been performed in quadrature, as each variable in question was independent.

Due to the relationships between energy transfer and defects produced, the higher energy bins in the reactor spectrum contribute substantially more to the defect total than the lower bins. This is further complicated by incident neutron energies > 3.4 MeV from the HFIR spectrum having low probabilities to be sampled, and presents a potentially large source of uncertainty in the defect total produced. In order to characterize the uncertainty potentially introduced by these high energy bins, a linear combination approach is used. 10^7 histories are simulated for each bin in the input spectrum to ensure sufficient statistical representation of each bin. Due to the energy transfer dependence of the defect calculation, each collision resulting from a given energy bin of index j must first be sorted into downscatter bins of index i.

The variation within bin downscatter bin i of source bin j is modeled by a Poisson distribution, and the uncertainty is quantified using the coefficient of variation [61],

$$CV_i = \sqrt{\frac{N}{(N-1)}\left[\frac{\sum_k \mu_{ki}^2(E)}{\left(\sum_k \mu_{ki}(E)\right)^2} - \frac{1}{N}\right]}. \tag{15}$$

Here each $\mu_{ki}(E)$ corresponds to the defects produced by a single neutron k of energy E within the ith downscattering bin of the jth source bin simulation. N corresponds to the number of neutrons which downscattered to that bin, and CV_i to the coefficient of variation for the ith downscattering bin. After determining all CV_i, CV_j is calculated using the following relationship:

$$CV_j = \frac{\sum_i CV_i \bar{\mu}_i}{\bar{\mu}_j} \tag{16}$$

First in this equation, the sum is computed of all CV_i times the average number of defects produced per collision for the ith downscatter bin, $\bar{\mu}_i$. Multiplying CV_i by $\bar{\mu}_i$ converts from relative error to absolute error for each bin. Working in absolute errors permits reliance on common uncertainty propagation relationships. In this case, the defect total for the source bin is the sum of defect totals for each downscatter bin, so the absolute errors of each downscatter bin may be summed to provide an estimate of the absolute error of the total. The final step, dividing by $\bar{\mu}_j$, or the average number of defects produced per neutron for the jth source bin, converts this absolute error back to relative. Once coefficients of variation are obtained for each source energy bin, each is projected against the source bin's associated sampling probability, p_j and summed as follows:

$$\delta = \sum_j p_j CV_j \tag{17}$$

Here, δ represents the relative uncertainty in the overall defect total produced by the linear combination of all source energy bin simulations, weighted according to the probabilities of the HFIR neutron energy spectrum. The resulting uncertainty is 0.91%. This is sufficiently low to conclude that the relative representation of bins does not contribute significantly to uncertainty in the final defect total.

Appendix E. Experiment Linearity

When viewing the experimental data in Fig. 8, they appear to adhere predominantly to a piece-wise linear relationship in log-log space. The experimental data are plotted in isolation in Fig. 18 with linear fits in log-log to investigate this observation. The data are broken up by the paper they were pulled from. Fig. 18 (a) shows the data from Chen et al., which appear to adhere strongly to the observed piece-wise linear relationship. By contrast, the data from Mcgowan and Sibley do not appear to exhibit two distinct linear relationships, instead more loosely appearing linear throughout. Plot (a) shows a more convincing fit overall than (b), with tighter data and two relatively strongly defined regions. It is suggested that the continuous linear appearance in (b) may be the result of outliers in the low dose region, where impurities in the sample dominate in concentration. This is discussed in more detail below. The relationship exhibited in (a) further suggests that saturation or annealing effects may onset earlier than predicted by the model, and that additional phenomena are involved.

Comparison of the slopes of the experimental fits and the defect algorithm in its linear region reveals a potential inaccuracy in the overall formulation of defect accumulation as a function of dose. Due to the log-scale nature of the region of interest, the fits were produced under log-scale and then exponentiated, making them nonlinear at low dose. The slopes compared are the slopes in the region of interest. The slope of the model in its linear region is 10.87 cm^{-1}, while the slope of the low dose fit to the data in Fig. 18 (a) is 8.17 cm^{-1}. This indicates that the description of defect concentration in a material subject to low neutron dose as depending solely on a constant defect formation rate (dF/dt) is not fundamentally accurate; nevertheless, the model and the experimental data align closely in this regime. The particular reason for this behavior is unclear. Considering the model assumes zero defects exist

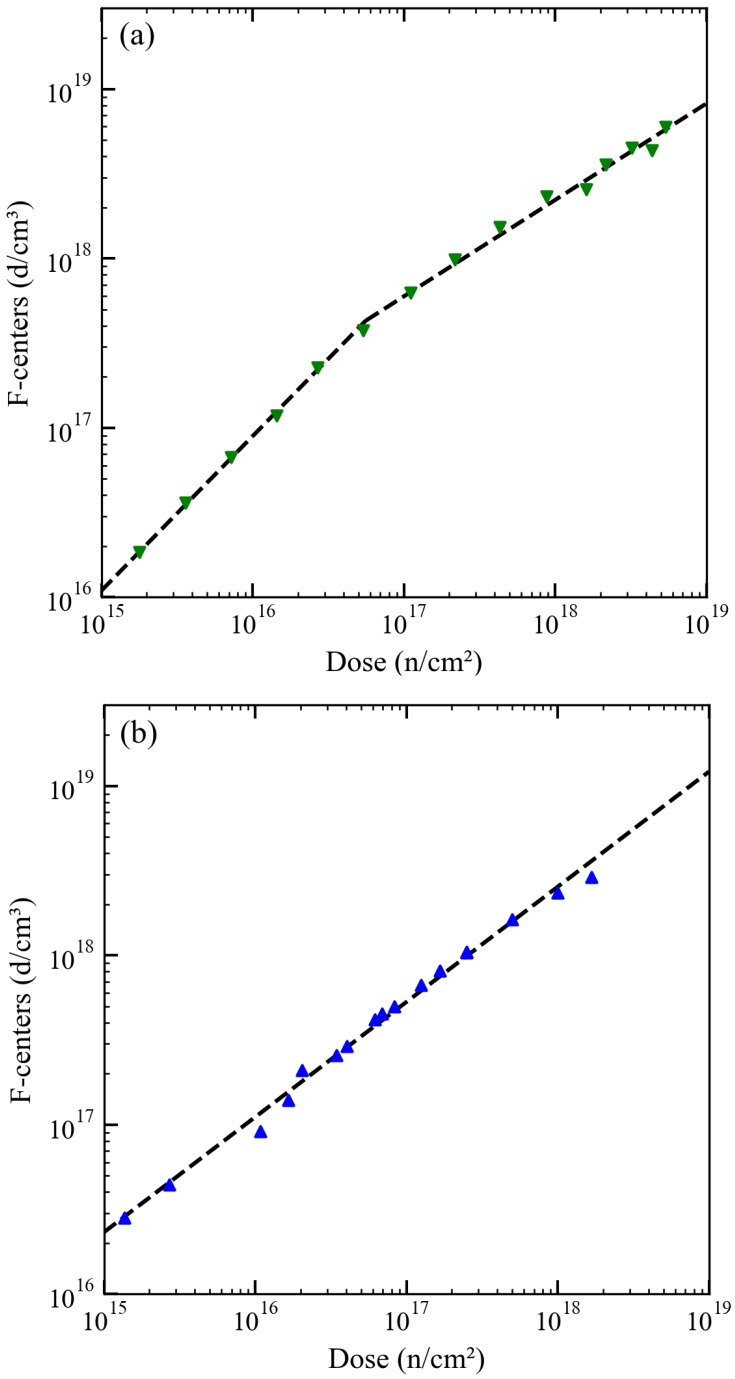

Figure 18: Linear fits applied to experimental data to showcase behavior in disagreement with the model. The data from Chen et al. (a) appear to agree strongly with a piece-wise linear relationship, while for Mcgowan and Sibley (b) they follow a continuous linear relationship with worse consistency.

at zero dose, it can be concluded from extrapolation of the experimental dose that some initial concentration of defects exists in the sample at zero dose. Due to the exponential nature of these fits, the precise value of the y-intercept cannot be accurately predicted, however its existence suggests that the experimental data and the model agree in the region of interest due to convergence from potentially vastly different starting values. One possible explanation is the model's basis on experimentally determined parameters and relationships - the region of agreement corresponds to a dose range well characterized by experiments. The phenomena responsible for this difference in slope are nevertheless unclear, however, and this observation warrants further investigation.

Bibliography

[1] K. Nordlund, S. J. Zinkle, A. E. Sand, F. Granberg, R. S. Averback, R. E. Stoller, T. Suzudo, L. Malerba, F. Banhart, W. J. Weber, F. Willaime, S. L. Dudarev, and D. Simeone, "Primary Radiation Damage: A Review of Current Understanding and Models," *J. Nucl. Mater.*, vol. 512, pp. 450–479, 2018, ISSN: 0022-3115. DOI: 10.1016/j.jnucmat.2018.10.027.

[2] A. J. Samin and J. C. Petrosky, "An Analysis of Point Defects in ZnTe Using Density Functional Theory Calculations," *J. Alloys Compd.*, vol. 921, no. 166017, 2022. DOI: 10.1016/j.jallcom.2022.166017.

[3] N. J. Quartemont, G. Peterson, C. Moran, A. J. Samin, B. Wang, C. Yeamans, B. Woodworth, D. Holland, J. C. Petrosky, and J. E. Bevins, "ATHENA: A Unique Radiation Environment Platform at the National Ignition Facility," *Nucl. Instrum. Methods in Phys. Res. A*, vol. 1016, no. 165777, 2021. DOI: 10.1016/j.nima.2021.165777.

[4] A. Samin and L. Cao, "Monte Carlo Study of Radiation-Induced Demagnetization Using the Two-Dimensional Ising Model," *Nucl. Inst. Methods in Phys. Res. B*, vol. 360, pp. 111–117, 2015, ISSN: 0168-583X. DOI: 10.1016/j.nimb.2015.08.067.

[5] A. J. Samin, D. A. Andersson, E. F. Holby, and B. P. Uberuaga, "On the role of electro-migration in the evolution of radiation damage in nanostructured ionic materials," *Electrochem. Commun.*, vol. 96, pp. 47–52, 2018, ISSN: 1388-2481. DOI: 10.1016/j.elecom.2018.09.010.

[6] J. E. Wertz, J. W. Orton, and P. Auzins, "Electron Spin Resonance Studies of Radiation Effect in Inorganic Solids," *Faraday Discuss.*, pp. 140–150, 1961. DOI: 10.1039/DF9613100140.

[7] J. V. Sharp and D. Rumsby, "Electron Irradiation Damage in Magnesium Oxide," *Radiat. Eff.*, vol. 17, pp. 65–68, 1973. DOI: 10.1080/00337577308232599.

[8] L. E. Halliburton and L. A. Kappers, "Radiation-Induced Oxygen Interstitials in MgO," *Solid State Commun.*, vol. 26, pp. 111–114, 1978. DOI: 10.1016/0038-1098(78)90509-4.

[9] G. P. Pells, "The Temperature Dependence of the Threshold Displacement Energy in MgO," *Radiat. Eff.*, vol. 64, no. 1-4, pp. 71–75, 1982. DOI: 10.1080/00337578208222990.

[10] W. D. Kingery, "Effect of Low Temperature Neutron Irradiation and 20-400C Annealing on the Density and Lattice Parameters of Aluminum Oxide and Magnesium Oxide," *J. Nucl. Mater.*, vol. 24, pp. 21–33, 1967. DOI: 10.1016/0022-3115(67)90077-3.

[11] Y. Chen, R. T. Williams, and W. A. Sibley, "Defect Cluster Centers in MgO," *Phys. Rev.*, vol. 182, no. 3, pp. 960–964, 1969. DOI: 10.1103/PhysRev.182.960.

[12] W. Mcgowan and W. A. Sibley, "Hardening of MgO Single Crystals by Electron and Neutron Irradiation," *Phil. Mag.*, vol. 19, no. 161, pp. 967–976, 1969. DOI: 10.1080/14786436908225861.

[13] B. Henderson and D. H. Bowen, "Radiation Damage in Magnesium Oxide. I. Dose Dependence of Reactor Damage," *J. Phys. C: Solid State Phys.*, vol. 4, pp. 1487–1495, 1971. DOI: 10.1088/0022-3719/4/12/005.

[14] J. C. Bruce D. Evans and P. R. Malmberg, "Coloration Induced in MgO by Ne+ Bombardment," *Phys. Rev. B*, vol. 6, no. 6, pp. 2453–2462, 1972. DOI: 10.1103/PhysRevB.6.2453.

[15] L. E. Halliburton, L. A. Kappers, D. L. Cowan, F. Dravnieks, and J. E. Wertz, "Isotropic ESR Line of the V- Center in MgO at Room Temperature," *Phys. Rev. Lett.*, vol. 30, no. 13, pp. 607–610, 1973. DOI: 10.1103/PhysRevLett.30.607.

[16] L. E. Halliburton, D. L. Cowan, W. B. J. Blake, and J. E. Wertz, "Magnesium-25 Hyperfine Confirmation of the Localized-Ground-State Model of the V- Center in MgO," *Phys. Rev. B*, vol. 8, no. 4, pp. 1610–1616, 1973. DOI: 10.1103/PhysRevB.8.1610.

[17] R. L. Nelson and D. B. Hartley, "A Comparison of Defect Centres formed in Oxides by Explosive Shocking and High-Energy Radiation," *J. Chem. Soc., Dalton Trans.*, pp. 1596–1603, 1972. DOI: 10.1039/DT9720001596.

[18] R. Williford, R. Devanathan, and W. Weber, "Computer Simulation of Displacement Energies for Several Ceramic Materials," *Nucl. Instrum. Methods Phys. Rev. B*, vol. 141, pp. 94–98, 1998, ISSN: 0168-583X. DOI: 10.1016/S0168-583X(98)00066-4.

[19] B. P. Uberuaga, R. Smith, A. R. Cleave, F. Montalenti, G. Henkelman, R. W. Grimes, A. F. Voter, and K. E. Sickafus, "Structure and Mobility of Defects Formed from Collision Cascades in MgO," *Phys. Rev. Lett.*, vol. 92, no. 115505, Mar. 2004. DOI: 10.1103/PhysRevLett.92.115505.

[20] B. P. Uberuaga, R. Smith, A. R. Cleave, G. Henkelman, R. W. Grimes, A. F. Voter, and K. E. Sickafus, "Dynamical Simulations of Radiation Damage and Defect Mobility in MgO," *Phys. Rev. B*, vol. 71, no. 104102, 2005. DOI: 10.1103/PhysRevB.71.104102.

[21] B. Uberuaga, R. Smith, A. Cleave, G. Henkelman, R. Grimes, A. Voter, and K. Sickafus, "Exploring Long-Time Response to Radiation Damage in MgO,"

Nucl. Instrum. Methods Phys. Rev. B., vol. 228, pp. 260–273, 2005. DOI: 10.1016/j.nimb.2004.10.055.

[22] C. J. Ortiz and M. J. Caturla, "Dynamical Simulations of Radiation Damage and Defect Mobility in MgO," *Phys. Rev. B*, vol. 75, no. 184101, 2007. DOI: 10.1103/PhysRevB.75.184101.

[23] D. S. Aidhy, P. C. Millett, D. Wolf, S. R. Phillpot, and H. Huang, "Kinetically Driven Point-Defect Clustering in Irradiated MgO by Molecular-Dynamics Simulation," *Scr. Mater.*, vol. 60, pp. 691–694, 2009, ISSN: 1359-6462. DOI: 10.1016/j.scriptamat.2008.12.052.

[24] T. Goorley, M. James, T. Booth, F. Brown, J. Bull, L. Cox, J. Durkee, J. Elso, M. Fensin, R. A. Forster, J. Hendricks, H. G. Hughes, R. Johns, B. Kiedrowski, R. Martz, S. Mashnik, G. McKinney, D. Pelowitz, R. Prael, J. Sweezy, L. Waters, T. Wilcox, and T. Zukaitis, "Features of MCNP6," Joint International Conference on Supercomputing in Nuclear Applications and Monte Carlo 2013, Paris, France, Oct. 2013.

[25] [Online]. Available: https://www.eetimes.com/tsmc-plans-new-fab-for-3nm/.

[26] [Online]. Available: https://news.samsung.com/global/samsung-foundry-innovations-power-the-future-of-big-data-ai-ml-and-smart-connected-devices.

[27] A. A. Kohnert and B. D. Wirth, "Cluster Dynamics Models of Irradiation Damage Accumulation in Ferritic Iron Part II: Effects of Reaction Dimensionality," *J. Appl. Phys.*, no. 154306, 2015. DOI: 10.1063/1.4918316.

[28] A. A. Kohnert, B. D. Wirth, and L. Capolungo, "Modeling Microstructural Evolution in Irradiated Materials with Cluster Dynamics Methods: A Review,"

Comput. Mater. Sci., vol. 149, pp. 442–459, 2018. DOI: 10.1016/j.commatsci.2018.02.049.

[29] A. K. B. D. Wirth X. Hu and D. Xu, "Modeling Defect Cluster Evolution in Irradiated Structural Materials: Focus on Comparing to High-Resolution Experimental Characterization Studies," *J. Mater. Res.*, vol. 30, no. 9, pp. 1440–1455, 2015. DOI: 10.1557/jmr.2015.25.

[30] Y. Li and N. Ghoniem, "Cluster Dynamics Modeling of Irradiation Growth in Single Crystal Zr," *J. Nucl. Mater.*, vol. 540, no. 152312, 2020, ISSN: 0022-3115. DOI: 10.1016/j.jnucmat.2020.152312.

[31] G. Luck and R. Sizmann, "The Radiation Annealing of Frenkel Defects," *Phys. Stat. Sol.*, vol. 5, pp. 683–691, 1964. DOI: 10.1002/pssb.19640050322.

[32] G. H. Kinchin and R. S. Pease, "The Displacement of Atoms in Solids by Radiation," *Rep. Prog. Phys.*, vol. 18, p. 1, 1955. DOI: 10.1088/0034-4885/18/1/301.

[33] C. J. Werner, J. Armstrong, S. G. Mashnik, G. W. McKinney, F. B. Brown, M. E. Rising, G. E. McMath, J. S. Bull, C. Solomon, J. S. Hendricks, L. Casswell, A. Sood, D. B. Pelowitz, L. J. Cox, J. E. Sweezy, R. E. Prael, D. Dion, C. J. Werner, T. E. Booth, R. A. Forster, A. Zukaitis, M. R. James, J. T. Goorley, C. Anderson, M. L. Fensin, H. G. Hughes, J. S. Elson, T. A. Wilcox, J. Favorite, J. W. Durkee, B. C. Kiedrowski, R. Martz, and R. C. Johns, "MCNP User's Manual Code Version 6.2," *Los Alamos National Laboratory*, 2017. [Online]. Available: https://mcnp.lanl.gov/pdf_files/la-ur-17-29981.pdf.

[34] L. Pauling, "The Sizes of Ions and the Structure of Ionic Crystals," *J. Am. Chem. Soc.*, vol. 49, pp. 765–790, 1927. DOI: 10.1021/ja01402a019.

[35] A. Foderaro, *The Elements of Neutron Interaction Theory*. Cambridge, MA: The Massachusetts Institute of Technology Press, 1971.

[36] P. Rinard, D. Reilly, N. Ensslin, H. Smith, and S. Kreiner, *Passive Nondestructive Assay of Nuclear Materials*. Washington, DC: United States Nuclear Regulatory Commission, 1991.

[37] M. Chadwick, M. Herman, P. Obložinský, M. Dunn, Y. Danon, A. Kahler, D. Smith, B. Pritychenko, G. Arbanas, R. Arcilla, R. Brewer, D. Brown, R. Capote, A. Carlson, Y. Cho, H. Derrien, K. Guber, G. Hale, S. Hoblit, S. Holloway, T. Johnson, T. Kawano, B. Kiedrowski, H. Kim, S. Kunieda, N. Larson, L. Leal, J. Lestone, R. Little, E. McCutchan, R. MacFarlane, M. MacInnes, C. Mattoon, R. McKnight, S. Mughabghab, G. Nobre, G. Palmiotti, A. Palumbo, M. Pigni, V. Pronyaev, R. Sayer, A. Sonzogni, N. Summers, P. Talou, I. Thompson, A. Trkov, R. Vogt, S. van der Marck, A. Wallner, M. White, D. Wiarda, and P. Young, "ENDF/B-VII.1 Nuclear Data for Science and Technology: Cross Sections, Covariances, Fission Product Yields and Decay Data," *Nuclear Data Sheets*, vol. 112, no. 12, pp. 2887–2996, 2011, Special Issue on ENDF/B-VII.1 Library, ISSN: 0090-3752. DOI: https://doi.org/10.1016/j.nds.2011.11.002. [Online]. Available: https://www.sciencedirect.com/science/article/pii/S009037521100113X.

[38] R. D. Cheverton and T. M. Sims, "HFIR Nuclear Core Design," Oak Ridge National Laboratory, Oak Ridge, TN 37830, Tech. Rep. ORNL-4621, 1971. DOI: 10.2172/4008514.

[39] F. B. K. Kam and J. H. Swanks, "Neutron Flux Spectrum in the HFIR Target Region," Oak Ridge National Laboratory, Oak Ridge, TN 37830, Tech. Rep. ORNL-TM-3322, 1971. [Online]. Available: https://inis.iaea.org/collection/NCLCollectionStore/_Public/02/012/2012273.pdf.

[40] T. A. Gabriel, B. L. Bishop, and F. W. Wiffen, "Calculated irradiation response of materials using fission reactor (HFIR, ORR, and EBR-II) neutron spectra," Aug. 1979. DOI: 10.2172/5968308. [Online]. Available: https://www.osti.gov/biblio/5968308.

[41] I. Remec and F. B. Kam, "Neutron Spectra at Different High Flux Isotope Reactor (HFIR) Pressure Vessel Surveillance Locations," Oak Ridge National Laboratory, Oak Ridge, TN 37830, Tech. Rep. ORNL-TM-12484, 1979. DOI: 10.2172/140411.

[42] A. Bergeron, "Review of the Oak Ridge National Laboratory (ORNL) Neutronics Calculations Regarding the Conversion of the High Flux Isotope Reactor (HFIR) to the Use of Low Enriched Uranium (LEU) Fuel," Argonne National Laboratory, Lemont, IL 60439, Tech. Rep. ANL/RERTR/TM-12/49, 2012. DOI: 10.2172/1060155.

[43] T. V. Blosser and G. E. T. Jr., "Neutron Flux and Neutron and Gamma-Ray Spectra Measurements at the HFIR", institution = "Oak Ridge National Laboratory," Oak Ridge, TN 37830, Tech. Rep. ORNL-TM-2221, 1968. [Online]. Available: https://www.osti.gov/servlets/purl/4492768.

[44] A. Bisson, "Etude au microscope electronique des defauts de structure dans l'oxyde de beryllium fritte irradie," *J. Nucl. Mater.*, vol. 10, no. 4, pp. 321–328, 1963. DOI: 10.1016/0022-3115(63)90183-1.

[45] W. A. Sibley and Y. Chen, "Radiation Damage in MgO," *Phys. Rev.*, vol. 160, pp. 713–716, 1967. DOI: 10.1103/PhysRev.160.712.

[46] J. D. Konitzer and J. J. Markham, "Experimental Study of the Shape of the F-Band Absorption in KCl," *J. Chem. Phys.*, vol. 32, p. 843, 1960. DOI: 10.1063/1.1730807.

[47] D. Y. Smith and G. Graham, "Oscillator Strengths of Defects in Insulators: The Generalization of Smakula's Equation," *J. Phys., I*, vol. C6, 1980. DOI: 10.1051/jphyscol:1980621.

[48] E. Cashwell, J. R. Neergeard, W. M. Taylor, and G. D. Turner, "MCN: A Neutron Monte Carlo Code," Los Alamos National Laboratory, Los Alamos, NM 87544, Tech. Rep. LA-4751, 1972. DOI: 10.2172/4497077.

[49] Y. Chen, D. L. Trueblood, O. E. Schow, and H. T. Tohver, "Color Centers in Electron Irradiated MgO," *J. Phys. C: Solid St. Phys.*, vol. 3, pp. 2501–2508, 1970. DOI: 10.1088/0022-3719/3/12/016.

[50] B. Park, W. J. Weber, and L. R. Corrales, "Molecular Dynamics Study of the Threshold Displacement Energy in MgO," *Nucl. Instr. and Meth. in Phys. Rev. B*, vol. 166-167, pp. 357–363, 2000. DOI: 10.1016/S0168-583X(99)00694-1.

[51] L. Kittiratanawasin, R. Smith, B. P. Uberuaga, and K. Sickafus, "Displacement Threshold and Frenkel Pair Formation Energy in Ionic System," *Nucl. Instrum. Methods. Phys. Res. B*, vol. 268, pp. 2901–2906, 2010. DOI: 10.1016/j.nimb.2010.04.024.

[52] M. J. Norgett, M. T. Robinson, and I. M. Torrens, "A Proposed Method of Calculating Displacement Dose Rates," *Nucl. Eng. Des.*, vol. 33, pp. 50–54, 1975. DOI: 10.1016/0029-5493(75)90035-7.

[53] R. E. Stoller, S. I. Golubov, C. Domain, and C. S. Becquart, "Mean Field Rate Theory and Object Kinetic Monte Carlo: A Comparison of Kinetic Models," *J. Nucl. Mat.*, vol. 382, pp. 77–90, 2008. DOI: 10.1016/j.jnucmat.2008.08.047.

[54] J. Marian and V. V. Bulatov, "Stochastic Cluster Dynamics Method for Simulations of Multispecies Irradiation Damage Accumulation," *J. Nucl. Mat.*, vol. 415, pp. 84–95, 2011. DOI: 10.1016/j.jnucmat.2011.05.045.

[55] M. Kiritani, "Analysis of the Clustering Process of Supersaturated Lattice Vacancies," *J. Phys. Soc. Jpn.*, vol. 35, pp. 95–107, 1973. DOI: 10.1143/JPSJ.35.95.

[56] S. I. Golubov, A. M. Ovcharenko, A. V. Barashev, and B. N. Singh, "Grouping Method for the Approximate Solution of a Kinetic Equation Describing the Evolution of Point-Defect Clusters," *Phil. Mag. A*, vol. 81, pp. 643–658, 2001. DOI: 10.1080/01418610108212164.

[57] D. Pooley, "The Saturation of F-Centre Production in Alkali Halides Under Proton Irradiation," *Br. J. Appl. Phys.*, vol. 17, pp. 855–861, 1966. DOI: 10.1088/0508-3443/17/7/303.

[58] S. Sikhoruchkin, Z. Soroko, A. Sukhovoj, and V. Khitrov, *Excited Nuclear States: Subvolume A Nuclei with Z = 1 - 29*. Berlin/Heidelberg, Germany: Springer, 2012.

[59] A. Pietropaolo, M. Angelone, R. Bedogni, N. Colonna, A. Hurd, A. Khaplanov, F. Murtas, M. Pillon, F. Piscitelli, E. Schooneveld, and K. Zeitelhack, "Neutron detection techniques from μeV to GeV," *Phys. Rep.*, vol. 875, pp. 1–65, 2020. DOI: 10.1016/j.physrep.2020.06.003.

[60] L. A. Bernstein, D. A. Brown, A. J. Koning, B. T. Rearden, C. E. Romano, A. A. Sonzogni, A. S. Voyles, and W. Younes, "Our Future Nuclear Data Needs," *Annu. Rev. Nucl. Part.*, vol. 69, pp. 109–136, 2019. DOI: 10.1146/annurev-nucl-101918-023708.

[61] I. Lux and L. Koblinger, *Monte Carlo Particle Transport Methods: Neutron and Photon Calculations", publisher = "CRC Press*. Boca Raton, Florida, Oct. 1991.

REPORT DOCUMENTATION PAGE

Form Approved
OMB No. 0704–0188

1. REPORT DATE *(DD–MM–YYYY)*	2. REPORT TYPE	3. DATES COVERED *(From — To)*
24-02-2023	Master's Thesis	Sep 2021 - Mar 2023

4. TITLE AND SUBTITLE

Fast Engineering Model for Defect Production in Magnesium Oxide

5a. CONTRACT NUMBER

5b. GRANT NUMBER

5c. PROGRAM ELEMENT NUMBER

6. AUTHOR(S)

Little, Henry, Civ

5d. PROJECT NUMBER

5e. TASK NUMBER

5f. WORK UNIT NUMBER

7. PERFORMING ORGANIZATION NAME(S) AND ADDRESS(ES)

Air Force Institute of Technology
Graduate School of Engineering and Management (AFIT/EN)
2950 Hobson Way
WPAFB OH 45433-7765

8. PERFORMING ORGANIZATION REPORT NUMBER

AFIT-ENP-MS-23-M-094

9. SPONSORING / MONITORING AGENCY NAME(S) AND ADDRESS(ES)

10. SPONSOR/MONITOR'S ACRONYM(S)

11. SPONSOR/MONITOR'S REPORT NUMBER(S)

12. DISTRIBUTION / AVAILABILITY STATEMENT

DISTRIBUTION STATEMENT A:
APPROVED FOR PUBLIC RELEASE; DISTRIBUTION UNLIMITED.

13. SUPPLEMENTARY NOTES

14. ABSTRACT

Defect production from irradiation of materials with thicknesses much less than the mean free path for neutron interaction is explored. A model is developed using the Monte Carlo N-Particle transport code from Los Alamos National Laboratory, experimental data from irradiations at the Oak Ridge High Flux Isotope Reactor, defect production theory, and atomistic simulation results to predict the total number of F-centers resulting from neutron irradiation of a MgO rod. This model accurately predicts the concentration of atomic defects under conditions closely matching experiments at long timescales, for large geometries, and requiring only 6.9 minutes on a single CPU. Results show agreement with experimental data between a factor of one to two depending on dose. Defect saturation is identified as the most likely source of disagreement. Inelastic scattering is identified as a large source of error for neutron energies > 1 MeV. The accuracy and computational performance achieved in this study shows great promise for future development of this technique and unifying the large gap between experimental data and simulation predictions of atomic defects.

15. SUBJECT TERMS

16. SECURITY CLASSIFICATION OF:			17. LIMITATION OF ABSTRACT	18. NUMBER OF PAGES	19a. NAME OF RESPONSIBLE PERSON
a. REPORT	b. ABSTRACT	c. THIS PAGE			Dr. Chris Lenyk, AFIT/ENP
U	U	U	UU	111	19b. TELEPHONE NUMBER *(include area code)*